Static and dynamic properties of two-dimensional Coulomb clusters

Biswarup Ash,[1] J. Chakrabarti,[2] and Amit Ghosal[1]
[1]*Indian Institute of Science Education and Research, Kolkata, Mohanpur 741246, India*
[2]*S.N. Bose National Centre for Basic Sciences, Block JD, Sector III, Salt Lake, Kolkata 700098, India*
(Received 28 January 2017; revised manuscript received 16 July 2017; published 5 October 2017)

We study the temperature dependence of static and dynamic responses of Coulomb interacting particles in two-dimensional confinements across the crossover from solid- to liquid-like behaviors. While static correlations that investigate the translational and bond orientational order in the confinements show the footprints of hexatic-like phase at low temperatures, dynamics of the particles slow down considerably in this phase, reminiscent of a supercooled liquid. Using density correlations, we probe long-lived heterogeneities arising from the interplay of the irregularity in the confinement and long-range Coulomb interactions. The relaxation at multiple time scales show stretched-exponential decay of spatial correlations in irregular traps. Temperature dependence of characteristic time scales, depicting the structural relaxation of the system, show striking similarities with those observed for the glassy systems, indicating that some of the key signatures of supercooled liquids emerge in confinements with lower spatial symmetries.

DOI: 10.1103/PhysRevE.96.042105

I. INTRODUCTION

Long-range interacting classical particles in disordered media can give rise to exotic phases, e.g., hexatic glass [1], which is characterized by short-range positional order and quasi-long-range orientational order. The signature of this phase is similar to the usual hexatic phase discussed by Kosterlitz and Thouless [2,3] and Halperin, Nelson, and Young (KTHNY) [4–6] upon melting of a two-dimensional (2D) solid, but in the presence of quenched disorder. There have been attempts to understand experiments with colloidal particles [7], binary alloy [8], magnetic bubble lattice [9], and disordered type II superconductors [1] in light of hexatic glass. Though the existence of a true hexatic glass in the thermodynamic limit attracted critical theoretical debates [10,11], its signatures may be realized in small confined systems [12].

Finite systems, with small number of particles, are of great current interest. They generally offer controlled experimental tunability over a wide range of parameters. Disorder is inherent to all real materials and can be easily introduced in nanoclusters through the irregularities in their confinements. Small systems not only are significant from technological perspectives but also are very important from the angle of fundamental physics: They are an ideal playground for exploring the complex interplay of interactions and disorder [13,14]. In this paper, we develop an understanding of such interplay by studying static and dynamic correlations in nanoclusters with (long-range) Coulomb-interacting particles in different geometrical confinements. We set out to identify the signatures of the hexaticity and glassiness by studying these correlations.

Can the Coulomb particles in a trap undergo melting, akin to the melting of a Wigner crystal [15], its bulk counterpart? While a true phase transition pertains only to bulk systems, the notion of solid- and liquid-like "phases" has been used successfully to characterize qualitative behaviors of finite systems [16]. The solid-like phase of Coulomb clusters is called a Wigner molecule (WM) [17], as it mimics the physics of Wigner crystal [15].

In recent years, static and dynamic properties of two-dimensional (2D) Wigner molecues were studied for different types of confinements [18–22] and interaction potentials [19,23,24] across thermal melting. These theoretical studies are motivated by experimental realizations, such as colloidal suspensions [25–27], confined plasma [28–30], electrons in quantum dots in high magnetic fields [31,32], radio-frequency ion traps [33], and electrons on the surface of liquid helium [34]. In related studies, theoretical progress has been made to elucidate the interplay of Coulomb interaction and disorder [20,35,36] by tuning quantum fluctuations.

Thermal melting of a Wigner molecule also presents intriguing physical signatures, as originally demonstrated by Bedanov and Peeters [18]. Though an order-disorder thermal transition does not occur in 2D systems [37], KTHNY theory proposes a transition from a quasi-long-range ordered solid to an isotropic liquid, with an intervening hexatic phase that is characterized by short-range positional order and quasi-long-range bond-orientational order. Such a two-step melting scenario for clean 2D systems has been realized in experiments [38–40] and simulations [41,42]. The fate of such a description in the presence of disorder has drawn significant research interest [43–46]. Does the melting of 2D Coulomb interacting particles corroborate with the KTHNY melting, even in the absence of any disorder? In spite of thirty years of research, there is no definitive answer, to the best of our knowledge [47]. Recent studies of static [19] and dynamic [21] properties of confined Coulomb particles in an irregular trap, however, confirmed a thermal crossover from its solid- to liquid-like phases.

In fact, dynamics of particles across the melting often provides crucial insights [48] on thermal transitions, bringing out the intricacies of thermal phases. The dynamical response of 2D systems, close to the liquid-hexatic transition, show some striking similarities with that of liquids close to the glass transition [49]. Molecular dynamics simulations of 2D system of colloid particles [50] and experiments with granular materials [51,52] show that with the increase in orientational order, the dynamics of the particles slow down and become heterogeneous. Particles undergo a caging effect

(i.e., get temporarily trapped in the cage of its neighbors) and cooperative dynamics. These result in subdiffusive behavior of the mean square displacements, as observed in experiments [53] and simulations [54–56].

A study of spatiotemporal correlations [21] of Coulomb interacting particles in irregular and circular traps has recently unravelled features of intriguing and slow dynamics. Particles show qualitatively distinct motional footprints at different time scales. While at very short times dynamics is expectedly ballistic, it becomes strongly heterogeneous at intermediate and long times. At low temperature, some particles jiggle around their equilibrium positions, as expected in a solid, but others show spatially correlated motion in long and tortuous paths. This produces an exponential tail in the distribution of displacements, a ubiquitous feature of glass formers [57]. Such distributions show temporal crossover from a Gaussian to a variety of non-Gaussian behaviors, making progressively slow relaxations with time. Interestingly, such motion contributes to a stretched exponential (i.e., a decay slower than exponential) spatial relaxation, a signature of complex motion in a system of interacting particles in disordered media. A stretched Gaussian (i.e., decay is slower than Gaussian but higher than exponential) relaxation of particles has also been reported [21]. The non-Gaussian displacements were explained through a phenomenological model invoking dynamic heterogeneity causing a broad distribution of diffusivity in the clusters. Yet, the mean squared displacements of particles confirmed their Fickian motion.

In the backdrop of these surprising findings, some questions remain unanswered: How similar is the slow dynamics of Coulomb interacting particles in traps to that of supercooled systems? Can hexaticity be identified for Coulomb particles in confinements? Note that the existence of a true hexatic phase in a one-component plasma has been debated for a long time [47]. Does the low-temperature phase in irregular confinement signify a hexatic-glass phase by featuring partial signatures of both hexatic and glassy behaviors? What are the implications of heterogeneous dynamics on physical observables? Further, a heterogeneous dynamics signifies the presence of multiple time scales in the system. Can we extract different time scales for Coulomb clusters? How do the relaxation time scales depend on temperature? For a finite systems, dynamical responses get strongly affected by particle number and also by the geometry of the confinement. Can we extract any systematic dependence of the observables in clusters on their particle numbers, N?

We address the above questions by presenting, in this paper, the results of extensive computer simulations on the static and dynamic properties of Coulomb interacting particles in different confinement geometries. Melting in traps is mostly studied in confinements with circular symmetry [16,18,22], so that one can identify observables which can exploit this symmetry in identifying the melting. Here, we develop more general melting criteria that do not depend on spatial symmetry and hence should apply equally to irregular and circular traps.

Before moving to the technical details, we take this opportunity to summarize our results here. From our analysis of static properties, we find that while the positional order is depleted even at the lowest T for an irregular trap, a solid-like phase can still be identified due to the bond orientational order. A liquid-like phase emerges [19] with the breaking down of bond orientational order beyond a crossover temperature T_X; however, the inhomogeneities in the liquid in irregular confinement persists up to a much larger temperature, about an order of magnitude larger than T_X. Only beyond this large temperature scale ($\sim 10T_X$) does the system start to resemble a standard isotropic liquid. Our results are indicative of a hexatic-like low-temperature (T) phase in irregular confinement. In contrast, the positional and bond orientational order are better developed in circular confinement and show an isotropic liquid-like behavior at much lower temperature compared to that in irregular confinement. Interestingly, we find that the crossover temperature T_X is quite similar irrespective of the geometry of the confinement for systems with particle number $N > 100$. Analysis of the dynamical responses are found to be crucial in probing the intricacies of different thermal phases [48]. We find that while stretched exponential decay of the distribution of the displacement of particles persists, irrespective of N, for irregular confinement, it remains stretched Gaussian for circular confinement. The analysis of the trajectories of individual particles and temperature dependence of different time scales for irregular confinement show striking similarities to those observed for glass formers near the glass transition temperature [49].

The rest of the paper is organized as follows: In Sec. II, we will give the details of the models and methods used in our simulations, emphasizing the introduction of disorder through irregularity. We will also discuss our numerical methods. Then we present in Sec. III our results for static properties, where we analyze the thermal crossover through the temperature dependence of bond orientational order. In Sec. IV, dynamic properties are analyzed, by considering displacement of individual particles, time dependence of bond orientational correlation, and the temperature dependence of different characteristic time scales, such as structural relaxation time, persistence, and exchange times. Much of these pertain to quantifying any signature of a glass-like behavior. For both the static and dynamic properties, we study the dependence of our results on the system size. Finally, we conclude in Sec. V.

II. MODEL AND METHOD

We consider N classical particles each with charge q in a confining potential $V_{\rm conf}(r)$. These particles interact via long-range Coulomb potential and are restricted to move in a 2D plane. The Hamiltonian describing such a system reads as

$$\mathcal{H} = \frac{q^2}{\epsilon} \sum_{i<j=1}^{N} \frac{1}{|\vec{r}_i - \vec{r}_j|} + \sum_{i=1}^{N} V_{\rm conf}(r_i), \tag{1}$$

where $r_i = |\vec{r}_i| = \sqrt{x_i^2 + y_i^2}$ is the distance of the ith particle from the center. Here, the first term in the Hamiltonian represents Coulomb repulsion between particles in a medium with dielectric constant ϵ. We consider only the bare Coulomb repulsion, because systems with a small number of particles, particularly, in the presence of disorder, are expected to offer only a weak screening, if at all. In our study, we considered two types of confinement potential: (a) parabolic (having circular

symmetry),

$$V_{\rm conf}^{\rm Cr}(r) = \alpha r^2, \quad \text{where } \alpha = m\omega_0^2/2, \tag{2}$$

and (b) irregular (lacking all spatial symmetries) [19,58],

$$V_{\rm conf}^{\rm Ir}(r) = a\{x^4/b + by^4 - 2\lambda x^2y^2 + \gamma(x-y)xyr\}. \tag{3}$$

We will refer to the corresponding WMs as the circular Wigner molecule (CWM) and the irregular Wigner molecule (IWM), respectively. We hope that a comparative study of IWM and CWM will elucidate the role of disorder (through irregularity) on thermal crossover in finite systems.

We rescale the length $r' \to \phi^{1/3}\alpha^{-1/3}r$ and energy $E' \to \phi^{2/3}\alpha^{1/3}E$, where $\phi = q^2/\epsilon$, in such a way that the CWM Hamiltonian transforms to [18]

$$\mathcal{H}^{\rm Cr} = \sum_{i<j=1}^{N} \frac{1}{|\vec{r}_i - \vec{r}_j|} + \sum_i r_i^2 \tag{4}$$

and correspondingly the time scale will also be renormalized to $t' = \hbar\phi^{-2/3}\alpha^{-1/3}t$. Such renormalization of length, energy, and time will eventually make the temperature expressed as $T' = E'/k_B$, where k_B is the Boltzmann constant. In order to have an estimate of these new length and time scales in conventional units, we consider electrons in a GaAs heterostructure with a typical confinement energy of $\hbar\omega_0 =$ 1 meV. The above scaled length (r'), energy (E'), and time (t') unit takes the value of 630 Å, 1.7 meV, and 376 fs, respectively. In extracting these values, we have used, $q = -e$, the charge of an electron, $m = 0.067m_e$, the mass of an electron, and $\epsilon = 13$ [59].

$V_{\rm conf}^{\rm Cr}$ is quadratic in length scale while $V_{\rm conf}^{\rm Ir}$ is quartic. In order to facilitate a justified comparison between the two, we need to express the quartic irregular confinement in the units of quadratic circular confinement. This is achieved by setting the parameter $a = (m\omega_0^2/2r'^2)a'$, which includes both ω_0 and a scaling factor a', for irregular confinement. Thus a judicious choice of a', which now controls the strength of the irregular confinement, brings the two confinements on equal footing on dimensional ground. Following the same scale transformations as for the circular case, we obtain the following Hamiltonian for $V_{\rm conf}^{\rm Ir}$:

$$\mathcal{H}^{\rm Ir} = a'\left[\frac{x^4}{b} + by^4 - 2\lambda x^2y^2 + \gamma(x-y)xyr\right] + \sum_{1\leqslant i<j}^{N} \frac{1}{|\vec{r}_i - \vec{r}_j|}. \tag{5}$$

There is still the parameter, a', left to be fixed for $V_{\rm conf}^{\rm Ir}(r)$. For a given N, we choose the value of a' according to the following considerations.

We know that the model of a bulk 2D electron gas, neutralized by a uniform positive background, and interacting via Coulomb interaction, can be characterized by a single dimensionless coupling $\Gamma = \sqrt{\pi n}/T$, where n is the average number density [60]. Thus, for a given T, the thermodynamic properties of the system are completely determined by its density, n. In the present context of finite systems, we adopt the same view and assume that our systems are also characterized by the same parameter Γ (which we will justify below). In order to make a meaningful comparison between systems in different confinements but at same T and with same N, we fix the density by tuning a' for irregular confinement and α for circular confinement. The assumption of single parameter description in terms of Γ is later indicated (in Sec. III C) by its bulk value at melting, irrespective of N and trap geometries. Note that a' tunes the average density by making the quartic oscillator narrow or shallow. For a given N, we fixed the value of a' for the irregular confinement in such a way that the average interparticle distance is equal to that for circular confinement (which equates density in the two traps) at the lowest T. In this paper, we report results for $N = 75,150,$ and 500 particles, which require $a' = 0.10,0.055,$ and 0.020, respectively, following the above procedure.

The parameter λ in irregular confinement controls chaoticity in the single-particle dynamics [58]. Tuning λ from zero to unity generates periodic to chaotic motion of a single particle in the trap. Chaotic motion along with broken spatial symmetries are taken as the signatures of disorder in our study. The parameter $b(=\pi/4)$ breaks the symmetry of a square and γ breaks the reflection symmetry. We consider $\lambda \in [0.565,0.635]$ and $\gamma \in [0.10,0.20]$ [61]. The values of different parameters are adjusted to generate self-similar copies of motional signatures of a single particle in the system, and we collect statistics on observables over those realizations of disorder for the purpose of disorder averaging [62]. Results from CWM are averaged over many independent simulations.

To study the static properties, we carried out (classical) Metropolis Monte Carlo (MC) simulation [63] aided by a simulated annealing algorithm [64]. Dynamical responses are studied using molecular dynamics (MD) simulation [63]. To achieve a desired T, we have used Berendsen-like thermostat [63] during the equilibration. Once the equilibrium is achieved, a conventional velocity-Verlet algorithm [63] is used to integrate the equations of motion. We have performed MD runs up to 2×10^6 steps with a time step size of $dt = 0.005t'$. We find excellent match of different observables obtained from Monte Carlo simulation with the time-averaged results of those quantities obtained from molecular dynamics simulation. This is, however, true except for the lowest temperatures featuring slow dynamics, as we discuss below. The match of the physical results from the two independent methods validates the correctness of our findings.

III. STATIC PROPERTIES

The broken symmetry state of a system at low T can be identified by its order. For example, crystalline solid is characterized by both the (long-range) positional and orientational orders. We thus proceed to explore first the positional order in our systems at the lowest T. Note that even though translational symmetry is broken by confinements, a circularly confined system would still possess the azimuthal periodicity [18].

A. Positional order

We present in Fig. 1(a) the ground state ($T = 0$) configuration [65] in a specific irregular trap: $\lambda = 0.635, \gamma = 0.20$, for $N = 500$ particles. No positional order is apparent here

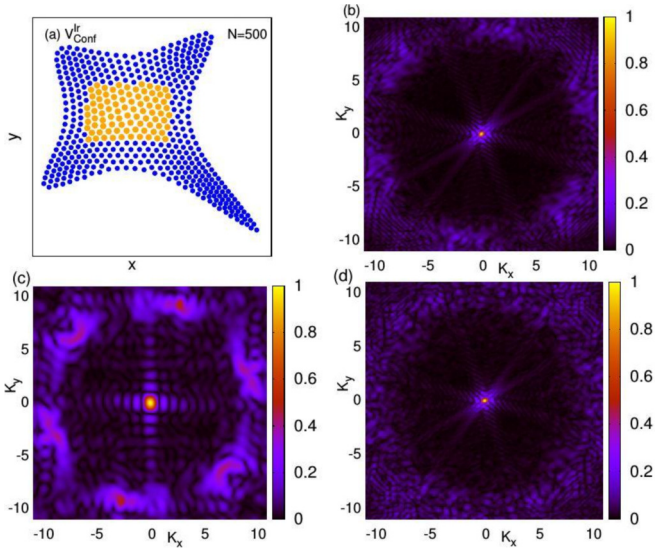

FIG. 1. (a) The ground-state ($T = 0$) configuration of $N = 500$ particles in an irregular trap ($\lambda = 0.635, \gamma = 0.20$). The orange dots are selected central particles for the search of positional order (see Sec. III A), while all other particles are represented by blue dots. Panels (b)–(d) show Fourier transforms of particle density for various cases: Panel (b) is for the ground state with all particles shown in panel (a). Panel (c) is for the orange particles only in the central region of panel (a). Panel (d) is for all particles, but at $T = 0.02 \sim T_X$, the crossover temperature. In panels (b)–(d), magnitude of $\rho(\vec{k})$ is scaled to unity for visual clarity.

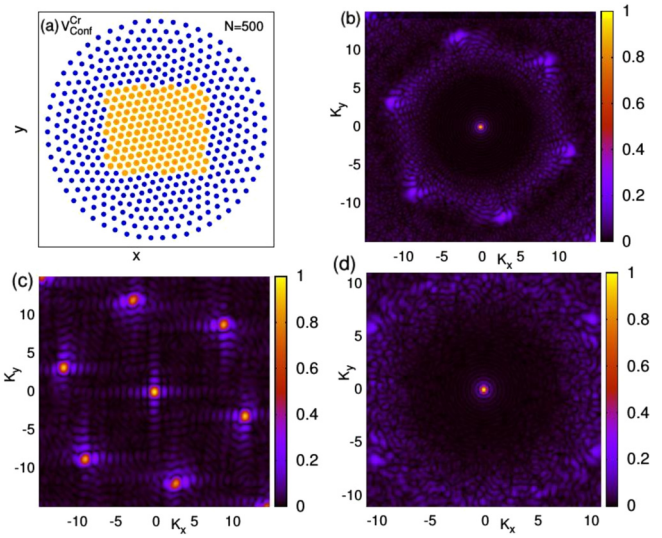

FIG. 2. (a) The ground-state ($T = 0$) configuration of $N = 500$ particles in circular confinement. The orange dots are particles in the central region selected to study positional order in the bulk, while all other particles are represented by blue dots. Panels (b)–(d) show Fourier transform of particle density for various cases: Panel (b) is for the ground state with all particles shown in panel (a). Panel (c) is for the particles only in the central region of panel (a). Panel (d) is for all particles, but at $T = 0.02 \sim T_X$. In panels (b)–(d), magnitude of $\rho(\vec{k})$ is scaled to unity for visual clarity.

to the naked eye. In order to quantify any ordering, we plot in Fig. 1(b) the Fourier component of local density, $\rho(\vec{k}) = \sum_{j=1}^{N} \exp[i\vec{k} \cdot \vec{r}_j]$, corresponding to the configuration shown in Fig. 1(a). Here, $\vec{k}$ is the momentum vector and $\vec{r}_j$ represents the position vector of the jth particle. We measure distances in the unit of r_0, the mean spacing between neighboring particles. For our choice of parameters, fixed by matching the density in the two traps, r_0 is the same for the IWM and CWM for a given N.

A perfect triangular lattice (the Bravais lattice for 2D Wigner crystal) shows Bragg peaks at the corresponding reciprocal lattice vectors, $\vec{k}_{\mathrm{RLV}}$. These peaks broaden with T, disappearing upon melting. In Fig. 1(b), we see only a weak diffuse pattern around $\vec{k}_{\mathrm{RLV}}$ in addition to strong peak at $\vec{k} = 0$. Broadness of these patches ensures that there is, at best, a very short range (much shorter than the system size) positional order in IWM. Because the positional order is expected to be weak near the boundary, we next look for such ordering for the particles near the central region of the trap. We choose only those particles (colored orange) which belong to a small region (of length $l_x = 7r_0$ along the x axis and $\sqrt{3}l_x/2$ along the y axis to accommodate a commensurate triangular lattice structure; see Appendix A for more details) near the center and study their contribution to $\rho(\vec{k})$. While the diffuse patches become more prominent, they hardly produce Bragg peaks; see Fig. 1(c). This finding, in addition to nearly no temperature dependence of $\rho(\vec{k})$ [as seen by comparing Fig. 1(b) at $T = 0$ and Fig. 1(d) at $T = 0.020$] comprise a strong signature of lack of any positional order in our IWM.

A CWM, in contrast, posses stronger positional order because of its azimuthal periodicity. This is reflected in Fig. 2, whose each panel depicts the same observables as in Fig. 1 but for CWM. The enhanced positional order is evident from Fig. 2(b) and particularly Fig. 2(c). The spatial extent of central particles is fixed by looking into the radial distribution, $n(r)$, of the $N = 500$ particles in CWM at the lowest $T(= 0.002)$ (for more details, see Appendix A). The depletion of positional order in this case is also evident by contrasting the T dependence in Figs. 2(b) and 2(d).

In the absence of appreciable positional order, solidity in IWM is contributed by the orientational order in 2D. Motivated by this assertion, we next analyze the bond orientational order in the system.

B. Bond orientational order

The bond orientational order parameter, $\psi_6(k)$, for kth particle is defined as [66]

$$\psi_6(k) = \frac{1}{N_b} \sum_{l=1}^{N_b} e^{i6\theta_{kl}}. \tag{6}$$

Here, θ_{kl} is the angle made by the bond between the particles k and l with an arbitrary axis and N_b is the number of nearest neighbors of particle k. We identify the nearest neighbours of a given particle by the standard Voronoi construction [67].

Physically, $|\psi_6|$ gives the propensity of a regular six-coordinated neighborhood of the chosen particle in its environment. Note that here $|\psi_6|$ is constructed to emphasize the bond orientational order in a triangular lattice which is often the Bravais lattice for interacting particles in 2D. A healthy

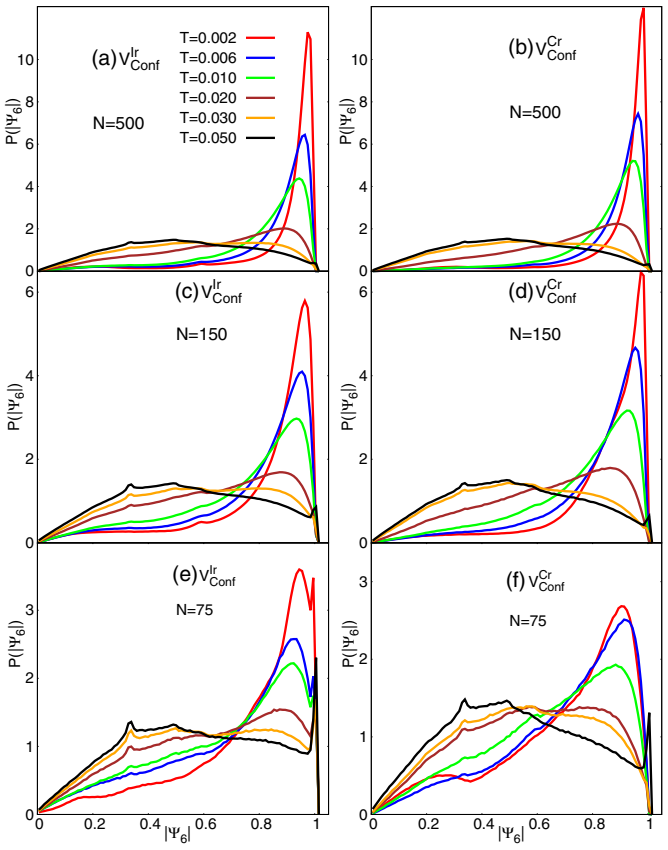

FIG. 3. Evolution of the the distribution, $P(|\psi_6|)$, of bond orientational order, $|\psi_6|$, with T is shown for $N = 500$ in panels (a) and (b), for $N = 150$ in panels (c) and (d), and for $N = 75$ in panels (e) and (f) in irregular and circular confinements, respectively. The low-T peak in $P(|\Psi_6|)$ at $|\Psi_6| \sim 1$, that signifies the "solidity," smears out as the system undergoes the thermal crossover. The small and weak peak in $P(|\Psi_6|)$ at $|\Psi_6| \sim 1$ at high T, particularly for smaller N, is a spurious one (see text) and does not constitute bond orientational order.

propensity of a six-coordinated neighborhood is discernible for the IWM at $T = 0$ in Fig. 1(a), except obviously for the particles on the boundary.

Figure 3(a) shows the T dependence of the probability distribution, $P(|\psi_6|)$, of $|\psi_6|(= |\psi_6(k)|$ for $k = 1,2,\ldots,N)$ for IWM with $N = 500$ particles. We see that the distribution is sharply peaked around unity at low $T(= 0.002)$, implying the presence of an orientationally ordered phase. With increase in T, the peak broadens due to thermal fluctuations that distorts the bond angles θ_{kl} with the neighbors. For $T > 0.02$, we get a very broad distribution signifying the breakdown of orientational order. Thus, the T dependence of $P(|\psi_6|)$ captures a thermal crossover from an orientationally ordered solid-like phase to a disordered liquid-like phase in confined systems.

Thermal evolution of $P(|\psi_6|)$ for CWM with $N = 500$ particles is shown in Fig. 3(b). The low-T peak in $P(|\Psi_6|)$ is sharper for CWM compared to IWM, depicting a stronger bond orientaional order for circular confinement. This occurs due to the formation of an ordered triangular-lattice-like structure around the central region of the circular confinement at low T [68,69], as shown in Fig. 2(a). With increase in T, the strength of the peak at $|\Psi_6| \sim 1$ diminishes and we find a broad distribution, similar to what is observed for irregular confinement, for $T > 0.020$.

How does $P(|\psi_6|)$ change with N? Figures 3(c) and 3(d) show the T dependence of $P(|\psi_6|)$ for $N = 150$ particles in irregular and circular confinements, respectively. We see that the height of the peak around $|\psi_6| \sim 1$, at low T, decreases with smaller N, implying diminishing bond orientational order. While the thermal evolution of $P(|\psi_6|)$ for $N = 150$ is qualitatively similar to what we find in Figs. 3(a) and 3(b) for $N = 500$, we observe the appearance of a small and feeble peak in $P(|\psi_6|)$ near $|\psi_6| \sim 1$ and 0.3 for both the confinements. We assert that such peak is spurious and carries no physical significance. We will discuss this feature shortly.

It is interesting to note that $P(|\psi_6|)$ shows hardly any thermal evolution for $T > 0.02$. This is found to be true irrespective of the confinement geometry. This insensitivity confirms that the scrambling of orienational order and hence melting is complete by $T \approx 0.03$.

With further decrease in N, we see some nongeneric features in the thermal evolution of $P(|\psi_6|)$. Figures 3(e) and 3(f) show the T dependence of $P(|\psi_6|)$ for $N = 75$ particles in irregular and circular confinements, respectively. Here, $P(|\psi_6|)$ not only loses its sharpness around $|\psi_6| = 1$ at low T but we also find the strengthening of the small peak near $|\psi_6| = 1$ at higher T for both the confinements. This spurious peak (as well as a similar weaker feature mentioned for $N = 150$), does not correspond to sixfold orientational order, as mentioned above. Note that a particle with a sole neighbor must yield $|\psi_6| = 1$, irrespective of the value of bond angle. And we find that the spurious peaks are contributed predominantly by the particles on the boundary, having fewer neighbors than usual. Decrease in N increases the ratio of the number of boundary particles to bulk particles and enhances such spurious signals.

To quantify the weakening of bond orientational order with decreasing N at low T, we have computed the fraction of particles having $|\psi_6| \geqslant 0.9$, which is given by the area under the $P(|\psi_6|)$ vs $|\psi_6|$ curve for $0.9 \leqslant |\psi_6| \leqslant 1$ at $T = 0.002$. We find that as N changes from 75 to 500, this fraction varies from 35% to 68% for irregular confinement while it changes more rapidly, from 20% to 71%, for circular confinement.

From our overall study, we find that systems with $N < 100$ tend to show nonuniversal behavior, not only for $P(|\psi_6|)$ but also for other observables we describe below. On the other hand, systems with $N = 100$–500 describe generic behavior featuring qualitatively similar results.

The nature of melting by disrupting bond orientational order is usually tracked by studying the large-r behavior of bond orientational correlation function, $g_6(r) = \langle \psi_6(r)\psi_6^*(0)\rangle$. However, for finite systems with small number of particles, $g_6(r)$ is not much useful, because any trend in its r dependence is hard to discern [19] due to limited values of r in confinements.

C. Projection of bond orientational order

In order to get additional insights into the degree of local orientational order, we next look into the short distance

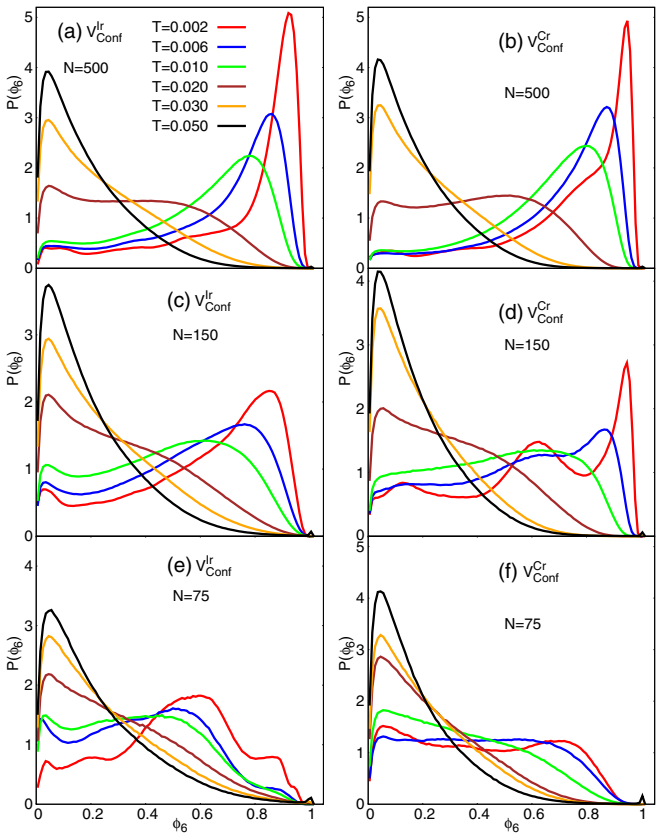

FIG. 4. Thermal evolution of the distribution, $P(\phi_6)$, of ϕ_6, representing the bond orientational correlation up to nearest neighboring distance (see text), is shown for $N = 500$ in panels (a) and (b), for $N = 150$ in panels (c) and (d), and for $N = 75$ in panels (e) and (f) in irregular and circular confinements, respectively. $P(\phi_6)$ features bimodal structures: The peak near $\phi_6 \sim 1$ (at low T) signals solidity, and the one at $\phi_6 \approx 0$ portrays liquidity.

projection of bond orientational correlation function, defined in the following way. The magnitude of this projection, $\phi_6(k)$, of the particle k, onto the average local bond orientational order of its nearest neighbors is defined as [70,71]

$$\phi_6(k) = \left| \psi_6(k)^* \frac{1}{N_b} \sum_{l=1}^{N_b} \psi_6(l) \right|. \tag{7}$$

While $|\psi_6(k)|$ measures the local hexagonal environment, $\phi_6(k)$ determines how the orientation of a particle fits into the mean orientation of its nearest neighbors. Thus, the distribution $P(\phi_6)$ represents the bond orientational correlation up to next nearest neighbor distances. At low T, as most of the particles are surrounded by regularly oriented six neighbors, we expect $\phi_6 \sim 1$. Increasing T depletes orientational order and ϕ_6 decreases to zero in a fully melted state.

We show in Fig. 4(a) the distribution $P(\phi_6)$ at different T for IWM with $N = 500$. At low $T(= 0.002)$, as expected the distribution $P(\phi_6)$ is sharply peaked at $\phi_6 \approx 1$. In contrast, at high $T(= 0.050)$, $P(\phi_6)$ becomes sharply peaked around $\phi_6 \sim 0$, implying the local sixfold order is lost even at the second shell, representing a liquid-like state.

Similar analysis for circular confinement with $N = 500$ particles [Fig. 4(b)] shows a sharper peak around $\phi_6 \sim 1$ in $P(\phi_6)$ at low T compared to irregular confinement. This reflects better orientational ordering in circular confinement due to azimuthal symmetry. But the qualitative features are similar in both confinements. It is interesting to note that the bimodal nature representing solid and liquid behavior crosses over at about $T_X = 0.02$ in both traps featuring a very flat distribution $P(\phi_6)$.

Lowering $N(= 150)$ [Fig. 4(c) for irregular and Fig. 4(d) for circular confinement] reduces the strength of the low-T peak at $\phi_6 \sim 1$, implying that the orientational correlation turns fragile with decreasing system size. This is unsurprising because of the increase of the fraction of boundary particles which naturally breaks orientational order. This is also reflected in the additional humps near $\phi_6 \sim 0$ at all temperatures for both confinements [Figs. 4(c) and 4(d)] and nongeneric multimodal $P(\phi_6)$ at low T for circular confinement, as seen in Fig. 4(d). Further reduction of N wipes out bond orientational correlation and a solid-like phase is hard to discern in irregular [Fig. 4(e)] or circular [Fig. 4(f)] confinements. Other than the peak in $P(\phi_6)$ near $\phi_6 \sim 0$ in both traps, the distribution features nongeneric behavior, making it difficult to discern a thermal crossover in smaller systems.

We extend our analysis to identify the crossover temperature, T_X, by studying the fluctuation of the orientational order parameters $|\psi_6|$ and ϕ_6, defined as

$$\chi_\psi = N[\langle|\psi_6|^2\rangle - \langle|\psi_6|\rangle^2], \tag{8}$$

$$\chi_\phi = N\left[\left\langle\phi_6^2\right\rangle - \langle\phi_6\rangle^2\right]. \tag{9}$$

Here, χ's are the generalized susceptibility correspond to order parameter $|\psi_6|$ and ϕ_6, respectively. A bulk system shows diverging susceptibility at the transition; however, they turn into a peak in finite systems whose sharpness increases with N. We identify the crossover temperature from the location of such peaks in χ_ψ and χ_ϕ.

We present the temperature dependence of χ_ψ for irregular and circular confinements in Figs. 5(a) and 5(b), respectively, for different N. The broad peak in ψ_6 in irregular confinement gets sharper with N; however, they all represent a unique $T_X \sim 0.02$. In contrast, the circular trap with $N = 75$ shows melting at a significantly lower T_X [Fig. 5(b)]. The qualitative physics carried by χ_ϕ, as presented in Figs. 5(c) and 5(d) for irregular and circular confinements, respectively, are similar to that of χ_ψ. For a system with small N, orientational melting swamps any radial ordering, resulting in a lower temperature for the disappearance of orientational order in our study.

The definitions of ϕ_6 and ψ_6 ensure $\phi_6(k) + |\psi_6(k)| \leqslant 2$. Further, being a projection, $\phi_6(k) \leqslant |\psi_6(k)|$. Hence, we can identify melting by describing each particle to be either solid- or liquid-like using the majority rule [70]: Particle k is solid-like if $\phi_6(k) + |\psi_6(k)| > 1$ and liquid-like otherwise. In Figs. 5(e) and 5(f), we show the fraction of solid- and liquid-like particles at different T for irregular and circular confinements, respectively. We see that at very low $T(= 0.002)$ almost 90% of the particles are solid-like, while at high $T(= 0.050)$ particles are mostly liquid-like. Interestingly, the two curves cross each other around the same T_X as obtained from other quantities mentioned above.

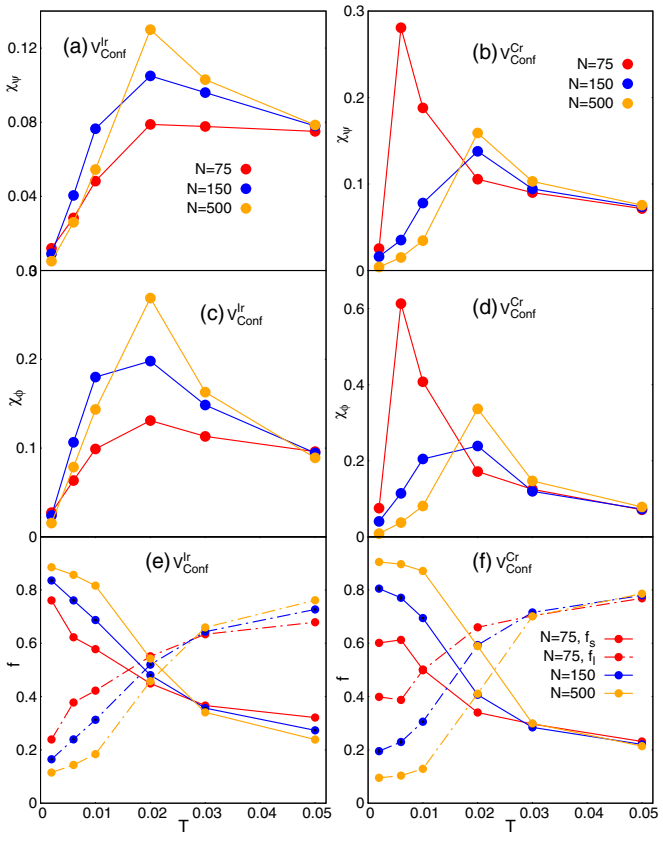

FIG. 5. T dependence of the generalized susceptibilities identifying the crossover temperature T_X, for $N = 500, 150, 75$. Panels (a) and (c) show the thermal evolution of χ_ψ and χ_ϕ respectively in irregular confinement. While the peaks of χ_ψ and χ_ϕ sharpen with N, their location, T_X, suffer hardly any change. Panels (b) and (d) show results similar to those in panels (a) and (c) but for circular trap. The fragile order in this case for $N = 75$ degrades T_X. Panels (e) and (f) illustrate the T dependence of the fraction of solid- and liquid-like particles in the system for circular and irregular trap. The crossing of the two takes place in a narrow window of T (for different N) for $V^{Ir}_{conf}(r)$, whereas the temperature window is broad for $V^{Cr}_{conf}(r)$.

In order to compare T_X with the corresponding melting temperature for bulk 2D systems, we also calculate the parameter $\Gamma(=\sqrt{\pi n}/T)$ at $T = T_X$. It is found that for bulk systems melting occurs for $\Gamma \approx 137$ [60] (see Appendix B for Γ at all T). In Table I, we show Γ for different N and

TABLE I. Estimation of the parameter $\Gamma = \sqrt{\pi n}/T_X$ characterizes the melting in bulk 2D systems, for irregular and circular confinements. For bulk systems, $\Gamma \approx 137$ at the transition. Note that the average particle density n is estimated by computing the area covered by N particles in the respective confinements.

	Irregular			Circular		
N	n	T_X	Γ	n	T_X	Γ
75	2.42	0.017 ± 0.003	162	1.90	0.011 ± 0.001	222
150	2.53	0.019 ± 0.001	148	2.12	0.019 ± 0.002	136
500	3.01	0.021 ± 0.001	146	2.78	0.020 ± 0.001	148

found that Γ remains close to 137, within acceptable tolerance for $N > 100$. Also, note that while Γ at T_X depends on N, it varies more widely for circular confinement than for irregular confinement.

Before moving to the next topic, the following point deserves a special mention here: A Wigner molecule with depleted positional order but featuring a healthy orientational order at length scale comparable to system size is indicative of hexaticity, expanding the notion of the KTHNY description. However, in systems with disorder, like the irregular confinement considered here, similar characteristics perhaps describe a hexatic glass phase. Our results in the preceding section indicates that a hexatic glass can be realized at least in the irregular trap.

IV. DYNAMIC PROPERTIES

In this section, we resort to dynamical characterization of different phases of our system. Some aspects of intriguing slow and heterogeneous dynamics in IWM with $N = 150$ have been recently reported [21] by us. Such a motion of constituent particles is a hallmark of glassy systems. Here, we expand on our earlier results, first by characterizing qualitatively the motional signatures in the traps and subsequently by extracting time scales associated with the structural relaxation causing the depletion of short-range bond orientational order in our amorphous system. We also explore the effect of particle number, N, on the dynamical characteristics of the system. At a given T, the dependence of each time correlation function on N for both the confinements is discussed in the appendix.

A. Temporal bond orientation correlation function

The long-time dynamical behavior of a system at different T can yield crucial information on the 2D phases of matter, e.g., solid, liquid, and hexatic phases [45,48]. Here, we first analyze the bond orientational correlation function in the time domain [45], defined as

$$g_6(t) = \langle \psi_6^*(t)\psi_6(0)\rangle. \tag{10}$$

In the solid phase, $g_6(t)$ remains constant in t, while it decays exponentially in the isotropic liquid phase for bulk systems. In the hexatic phase, $g_6(t)$ shows an algebraic decay, i.e., $g_6(t) \sim t^{-\alpha(T)}$ [48,66].

Figure 6(a) depicts the t dependence of $g_6(t)$ at different T with $N = 500$ particles in irregular confinement. Three distinct behaviors of $g_6(t)$ can be identified: At low T ($\leqslant 0.006$), $g_6(t)$ remains nearly flat, implying a solid-like phase. It decays exponentially in the high-T ($\geqslant 0.030$) liquid phase, whereas in the intermediate phase, $0.01 < T < 0.025$, we find that the decay is algebraic. We find $\alpha(T)$ to have a surprisingly weak T dependence across the whole intermediate-T region of its algebraic decay. The three distinct behaviors are also discernible in the circular trap as seen in Fig. 6(b). In contrast to IWM, $\alpha(T)$ shows a stronger T dependence in CWM. The robust power law decay of $g_6(t)$ is compelling evidence of the existence of a hexatic-like phase in our irregularly Coulomb clusters. Figures 6(c) and 6(d) show t dependence of $g_6(t)$ at different T with $N = 150$ particles in irregular and circular confinements, respectively. While we can still identify distinct

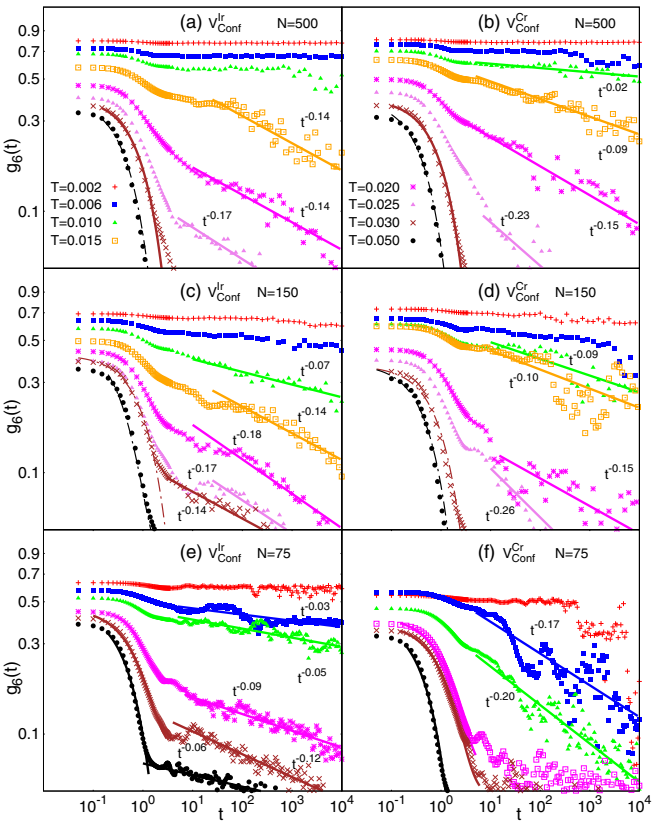

FIG. 6. t dependence of temporal bond orientational correlation function, $g_6(t)$, at different T for $N = 500$ [panels (a) and (b)], $N = 150$ [panels (c) and (d)], and $N = 75$ [panels (e) and (f)] particles in irregular and circular confinements, respectively. Solid lines are the appropriate fitting to the actual data (points). The results confirm three qualitatively different evolution: The low-T flat traces typify the solid-like behavior, the power-law decay for intermediate T is reminiscent of the bulk 2D hexatic trend, while the large temperature exponential fall represent isotropic liquid nature.

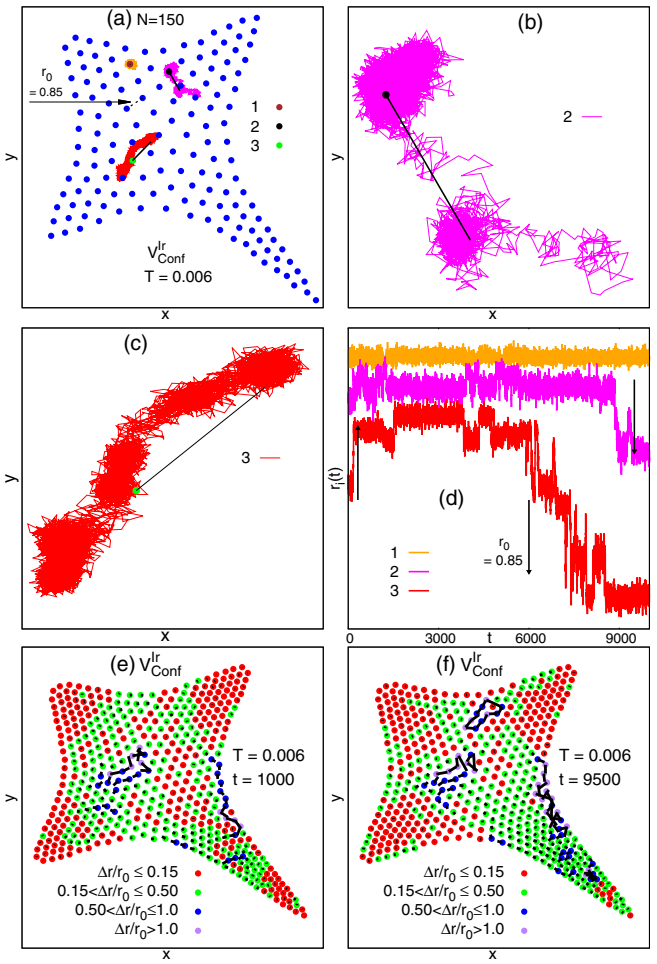

FIG. 7. (a) Initial positions of $N = 150$ particles (blue dots) in a specific realization of an irregular confinement along with the trajectories of three particles at $T = 0.006$. Thick black lines indicate the net displacement of the particles over the duration of the simulation. [(b), (c)] Trajectories of the particles 2 and 3 with larger displacements, as shown in panel (a). Both of them jiggle around their equilibrium position for a while and they make occasional and sudden jumps by distance $\sim r_0$. Particle 1, however, does not make such hops (not shown separately). (d) t dependence of the instantaneous distance $r_i(t)$ from the center of the confinement for the three selected particles ($i = 1,2,3$). Displacement ($\Delta\vec{r}_i(t) = \{\vec{r}_i(t) - \vec{r}_i(0)\}$) of $N = 500$ particles in irregular confinement is shown for (e) $t = 1000$ and (f) $t = 9500$ at $T = 0.006$.

temporal regimes for this smaller value of N, we do not find a time-independent $g_6(t)$ even at the lowest T. For $N = 75$, $g_6(t)$ decays more rapidly for $V^{\rm Cr}_{\rm conf}$ [Fig. 6(f)] compared to $V^{\rm Ir}_{\rm conf}$ [Fig. 6(e)] (see Appendix C for more details). For small N, the loss of bond orientation is swamped by azimuthal melting that typically occurs at a lower T [18].

B. Analysis of the trajectory

Focusing on a typical realization of the irregularity, $\{\lambda,\gamma\} = \{0.635,0.20\}$, we show in Fig. 7(a) the initial configuration of $N = 150$ particles (thick dots) at $T = 0.006$ after MD equilibration. On this, we also superimpose the trajectory of three particles (indexed as 1,2, and 3) during the MD simulations. We see that at low T the nature of the dynamics of individual particles can be broadly classified in following two categories:

(i) There are particles, like the one indexed 1 in Fig. 7(a), which only rattle around their equilibrium position over the duration of whole MD simulation.

(ii) Additionally, there are particles, indexed 2 and 3 in Fig. 7(a), which move longer distances (a few r_0) in the course of time. Their trajectories are enlarged in Figs. 7(b) and 7(c), along with a solid line representing the net displacement. These particles jiggle around their equilibrium position for certain time and then jump by a distance $\sim r_0$ and spend time there before jumping to previous (reversible motion) or to a new location (irreversible motion).

Such occasional jumps can be captured by looking into the instantaneous position, $r_i(t)$, as shown in Fig. 7(d), where i represents the particle index. We see that within a sufficiently small time window (and hence we call them jumps), these particles change their positions, moving by a distance of the order of r_0. This motion can be regarded as the cage-breaking process and avalanches of such cage-breaking

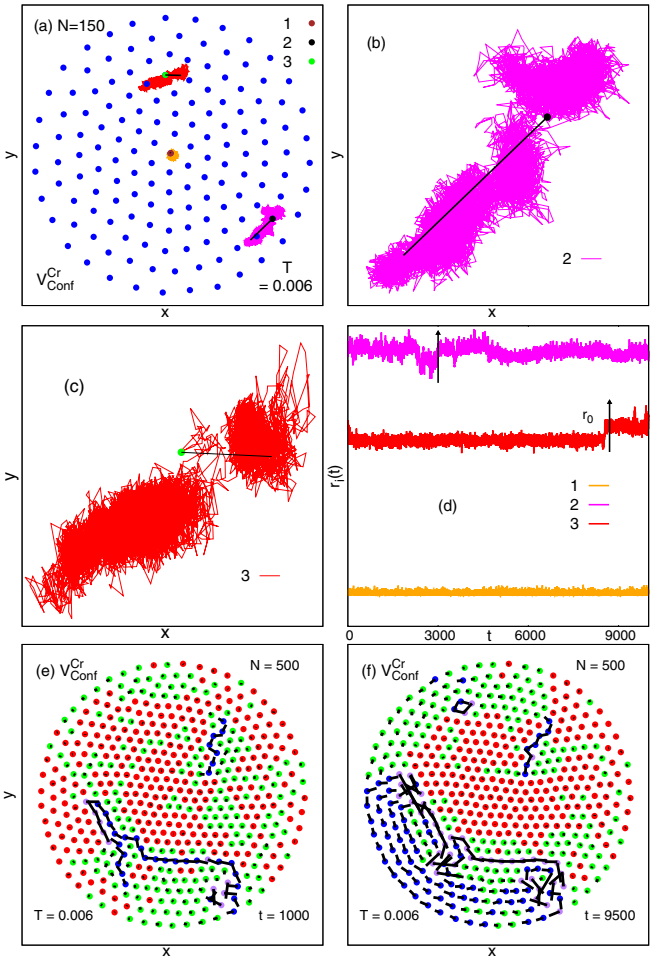

FIG. 8. (a) Initial positions of $N = 150$ particles (blue dots) in circular confinement along with the trajectories of three particles at $T = 0.006$. Solid lines indicate the net displacement of the particles over the duration of the simulation. [(b), (c)] Trajectories of the particles 2 and 3 with larger displacements, as shown in panel (a). (d) t dependence of the instantaneous distance $r_i(t)$ from the center of the confinement for the three selected particles ($i = 1,2,3$). Displacement $[\Delta\vec{r}_i(t)]$ of $N = 500$ particles in circular confinement is shown for (e) $t = 1000$ and (f) $t = 9500$ at $T = 0.006$.

events give rise to string-like pattern for the displacement $\Delta\vec{r}_i(t) = \{\vec{r}_i(t) - \vec{r}_i(0)\}$ of the particles as shown in Figs. 7(e) and 7(f) for $N = 500$. A similar trajectory for $N = 150$ was presented in Ref. [21]. We, however, note that the length of such string in the scale of system size decreases by going from $N = 150$ to $N = 500$, hinting that such motions are rare in the bulk limit. This cooperative motion in irregularly trapped Coulomb clusters is similar to those observed in other systems such as colloids [72], Lennard-Jones mixtures [56], and 2D dusty plasma [73]. Similar motional footprints have been found for each realization (identified by a specific pair of $\{\lambda,\gamma\}$) of irregular confinement we studied.

Figure 8 shows equivalent analysis for circular confinement, where Fig. 8(a) shows the initial configuration (thick dots) of $N = 150$ particles at $T = 0.006$ along with the trajectory of three selected particles. Trajectories of two particles are enlarged in Figs. 8(b) and 8(c). The instantaneous position $r_i(t)$ [Fig. 8(d)] in V^{Cr}_{conf} reveals that particles change their positions more gradually compared to those in V^{Ir}_{conf} [see Fig. 7(d)]. We find that particles in circular confinement also show heterogeneous dynamics [Figs. 8(e) and 8(f)]. However, the motions in this case are consistent with the azimuthal symmetry of the trap and hence the collective motion in a long and tortuous string-like path is less pronounced.

C. Inhomogeneity of the liquid beyond crossover

In our previous study [21], we found that the slow dynamics becomes profound near the thermal crossover. Here, the self-part of the Van Hove correlation [74], $G_s(r,t) = \langle\sum_{i=1}^{N}\delta[r - |\vec{r}_i(t) - \vec{r}_i(0)|]\rangle$, which represents the probability that a particle has moved by a distance r in time interval t, shows stretched exponential spatial decay at long times: $G_s(r,t) \sim \exp[-lr^{k(t)}]$ with $k < 1$. Here, we extend such studies to track the N dependence of $k(t)$ for different T. Henceforth, we denote k for V^{Ir}_{conf} and V^{Cr}_{conf} as k_{Ir} and k_{Cr}, respectively.

Figure 9(a) shows the t dependence of k_{Ir} at different T for $N = 500$. At low $T(\sim 0.006)$, k_{Ir} settles down to unity at intermediate and long t [inset of Fig. 9(a)], implying an exponential tail in $G_s(r,t)$. With increasing T, we find k_{Ir} drops below unity and attains the minimum value for around $T_X \sim 0.020$. For $T > T_X$, the long-time limit of k_{Ir} rises up again and only at a very high $T(= 0.250)$ k_{Ir} approaches 2, as expected for an isotropic liquid-like behavior.

Figures 9(b) and 9(c) depict the t dependence of k_{Ir} at different T for $N = 150$ and 75, respectively, and we see that while the stretched exponential behavior of $G_s(r,t)$ around T_X in V^{Ir}_{conf} is generic for all N, the finer details differ. In particular, the recovery of the final isotropic liquid-like behavior signaled by $k_{Ir} \to 2$ for large t occurs differently for different N. In Fig. 9(c), we see that an isotropic liquid is not at all recovered for $N = 75$ up to the largest time of our simulation, even at high $T(= 0.10)$. A system with $N = 500$ particles [Fig. 9(a)] attains such limit more smoothly than $N = 150$ [Fig. 9(b)], indicating a surprisingly large temperature window of inhomogeneous liquid (signaled by $k_{Ir} < 2$) would gradually shrink approaching the bulk limit. We find that k_{Ir} attains the minimum value (this value was found to increase with N) at $T \sim T_X$ for all N (see Appendix D for details).

Figure 10(a) depicts the t dependence of k_{Cr} for $N = 500$ at different T. While $k_{Cr} \approx 1$ at low T, we find $1 < k_{Cr} < 2$ at intermediate T and long t, implying that only a stretched Gaussian decay of $G_s(r,t)$ is realized in V^{Cr}_{conf} in contrast to the stretched exponential decay observed in V^{Ir}_{conf}. At higher $T(\geqslant 0.100)$, $k_{Cr} \sim 2$ for all t, describing an isotropic liquid-like behavior for all time scales. The stretched Gaussian decay of $G_s(r,t)$ persists even for smaller N, as shown in Fig. 10(b) for $N = 150$ and Fig. 10(c) for $N = 75$. It is worth mentioning here that recent experiments [75,76] with nanoparticles have realized such stretched Gaussian spatial decay in confined media. We note that while $k_{Cr} \to 2$ for $N = 75$, k_{Ir} fails to do so even at high T [Fig. 9(c)]. Thus, even though the solid phase is quite similar in circular and irregular geometry, the Coulomb liquid is quite inhomogeneous in irregular confinement for a much wider temperature range, $0.01 < T < 0.25$. Note that

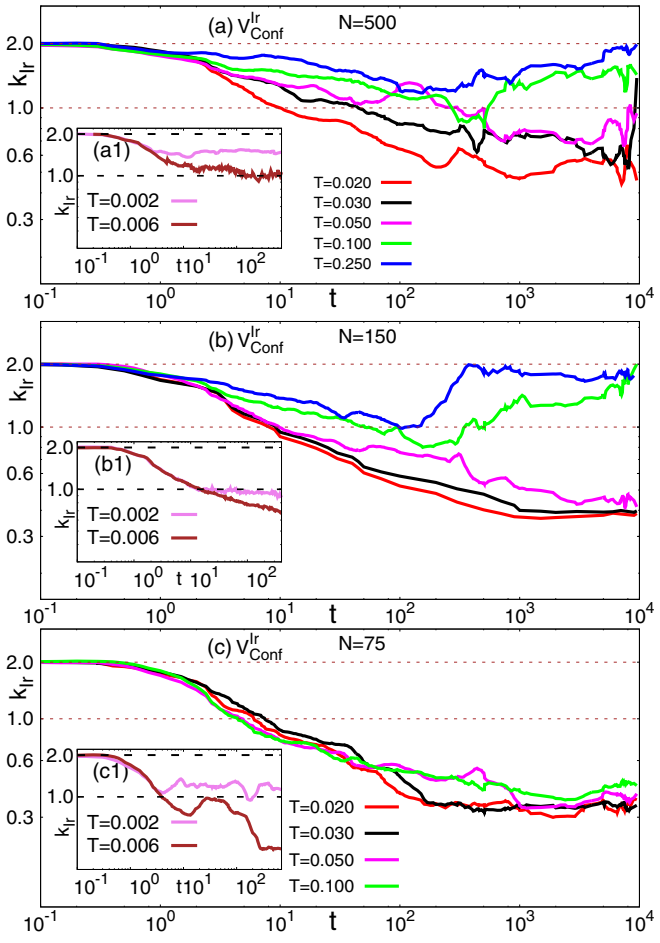

FIG. 9. Illustration of the intriguing spatial evolution of $G_s(r,t) \sim \exp[-lr^{k_{Ir}}]$ by depicting the t dependence of k_{Ir} (see text), at different T for V^{Ir}_{conf}. The results are analyzed for (a) $N = 500$, (b) $N = 150$, and (c) $N = 75$. Main panels show the t dependence of k_{Ir} beyond the crossover temperature, while the insets depict the t dependence of k_{Ir} at low T.

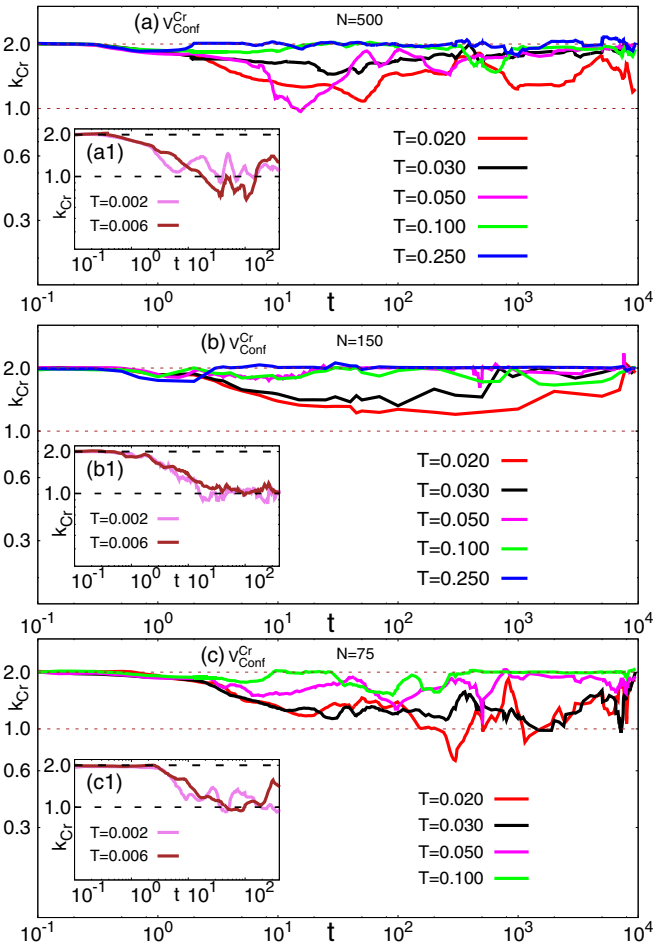

FIG. 10. t dependence of the exponent k_{Cr}, depicting the nature of the decay of $G_s(r,t)$ at different T for circular confinement, is analyzed for (a) $N = 500$, (b) $N = 150$, and (c) $N = 75$. Main panels show the t dependence of k_{Cr} beyond the crossover temperature, while the insets depict the t dependence of k_{Cr} at low T.

our results for the low Ts are consistent with the conjecture of universal exponential tails of $G_s(r,t)$ in glass formers [57] and hold even in the case of Coulomb clusters.

D. Time scales of structural relaxation

Motion in confined system is rife with heterogeneous dynamics, implying multiscale temporal relaxations. We focus below on extracting relevant time scales, e.g., structural relaxation time, cage correlation time, time scale of heterogeneity, and persistence and exchange times. We will also discuss how these signify the underlying dynamics, and finally we will compare all these time scales to understand the inter-relations among them.

1. Time scale for structural relaxation and heterogeneity

When particles in a solid diffuse, its structure relaxes, and we estimate the corresponding time scale for our systems in following manner. We calculate the time evolution of the self part of a two-point density correlation function, called the overlap function $Q(t)$ [77,78], defined as

$$Q(t) = \left\langle \frac{1}{N} \sum_{i=1}^{N} w(|\vec{r}_i(t_0 + t) - \vec{r}_i(t_0)|) \right\rangle, \qquad (11)$$

where $w(r) = 1.0$ if $r < r_c$ and zero otherwise. The angular parenthese denotes averaging of results over the time origin, t_0, over MD configurations, and also over different realizations of the disorder. Because particles mostly rattle in a small distance around their equilibrium positions (within r_c, as defined below) at small t, $Q(t) \sim 1$, whereas for large t, $Q(t) \sim 0$, signaling complete structural relaxation. Of course, the small size of t for the above statement depends on the operating T. We evaluate $w(r)$ by monitoring the displacements of individual particles. Once a particle moves by a distance greater than r_c, then we set $w(r) = 0$ for all future times, ensuring $Q(t)$ is a monotonically decaying function of t.

Obviously, $Q(t)$ depends on the choice of r_c and the optimal value of r_c is chosen so that the fluctuation of $Q(t)$ attains its maximum value (for details, see Appendix E). This fluctuation is quantified by dynamic susceptibility, $\chi_4(t) = \frac{1}{N}[\langle Q^2(t)\rangle - \langle Q(t)\rangle^2]$. At a given T, $\chi_4(t)$ attains maximum at a time, τ_χ,

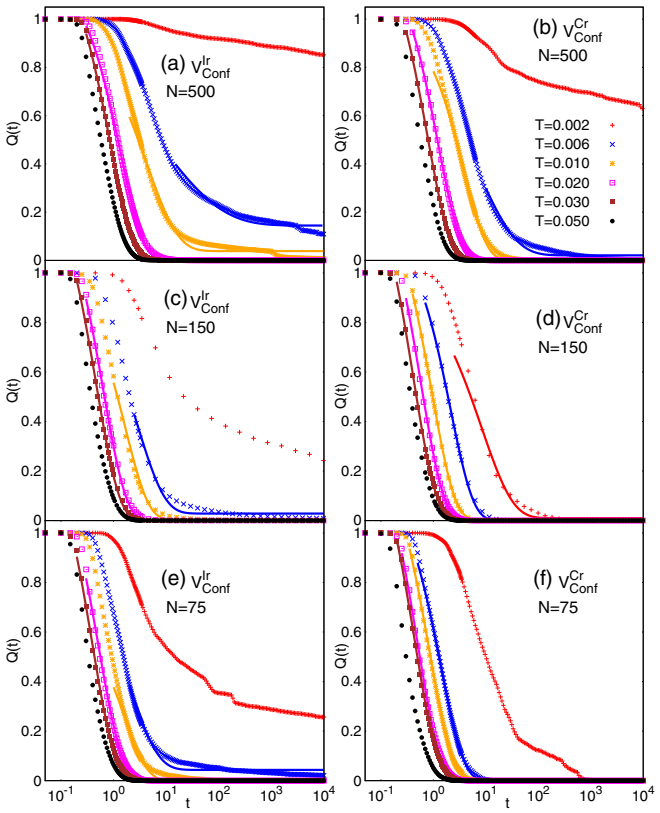

FIG. 11. The time dependence of the overlap function $Q(t)$ for different T for $N = 500$ [panels (a), (b)], $N = 150$ [panels (c), (d)], and $N = 75$ [panels (e), (f)] in irregular and circular confinements, respectively. Solid lines represent appropriate fitting of the data (points). While at low T, $Q(t)$ decays very slowly, it falls to zero rapidly for $T > 0.006$.

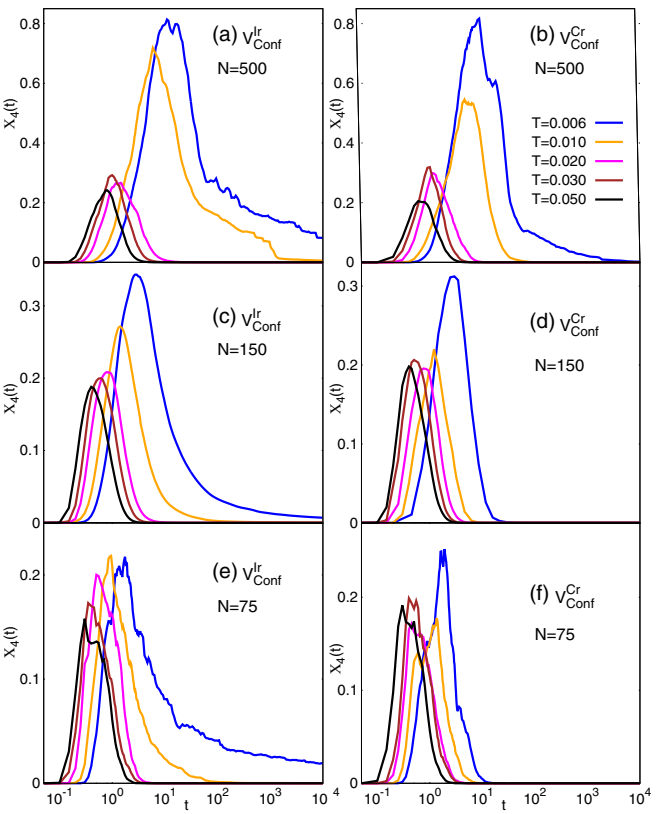

FIG. 12. The t dependence of $\chi_4(t)$ for different T for $N = 500$ [panels (a), (b)], $N = 150$ [panels (c), (d)], and $N = 75$ [panels (e), (f)] in irregular and circular confinements, respectively. For a given N, $\chi_4(t)$ attains maximum at time τ_χ which decreases with increase in T.

which is the time scale associated with dynamic heterogeneity [77,79].

Figure 11(a) shows the t dependence of $Q(t)$ in irregular confinement at different T for $N = 500$. While at low T, the decay of $Q(t)$ is very slow, and it falls to zero rapidly for $T > 0.010$. The time dependence is found to be of the form $Q(t) \propto \exp[-(t/\tau_\alpha)^c]$ [80], except for very short times. It is found to be exponential ($c = 1$) for $T > 0.010$, whereas it is stretched exponential for $T = 0.006$ and 0.010 and has a much slower decay for $T = 0.002$. Similar analysis for circular confinement with $N = 500$ [Fig. 11(b)] yields an exponential decay for $T > 0.006$ (see Appendix F for details) and stretched exponential for $T = 0.006$.

Figures 11(c) and 11(d) show t dependence of $Q(t)$ for irregular and circular confinements, respectively, with $N = 150$. With lower N we generally find that $Q(t)$ decays more rapidly at low T and shows stretched exponential decay for $T = 0.006$ in irregular confinement while it falls exponentially for circular confinement. At higher T, $Q(t)$ decays exponentially for both the confinements. For $N = 75$, we observe stretched exponential decay at $T = 0.006$ for irregular confinement [Fig. 11(e)], while $Q(t)$ decays exponentially for all higher T. For circular confinement, $Q(t)$ decays exponentially at all $T \geqslant 0.006$ [Fig. 11(f)]. Note that at low T, for any given N, $Q(t)$ decays faster for circular confinement compared to irregular confinement, implying that effect of disorder from the irregularity is to increase the structural relaxation time. Also, at any given T, $Q(t)$ decays more rapidly with decrease in N for both the confinements (see Appendix G for further details).

Next, we study the t dependence of $\chi_4(t)$ at different T. Figure 12(a) shows $\chi_4(t)$ at different T for irregular confinement with $N = 500$. $\chi_4(t)$ attains the maximum value at some intermediate time, τ_χ, which moves to lower value with increase in T. We find similar T dependence of $\chi_4(t)$ for circular confinement with $N = 500$ [Fig. 12(b)]. What happens if we decrease N? Figures 12(c) and 12(d) shows t dependence of $\chi_4(t)$ at different T for irregular and circular confinements, respectively, with $N = 150$. With decreasing N, we find that at any given T, τ_χ decreases to lower value, indicating that structural relaxation time decreases with N. Similar trends are also observed for $N = 75$ in two confinements [Figs. 12(e) and 12(f)].

We estimate the structural relaxation time, τ_α, using relation $Q(\tau_\alpha) = 1/e$ [77,79] for $T \geqslant 0.006$. For a bulk system, one generally estimates the structural relaxation time from the temporal decay of the self part of the intermediate scattering function, $F_s(k,t)$ [81] (with k set to the value at which the static structure factor features its first peak). But, since k is ill defined for a small finite system, we resort to $Q(t)$ for estimating τ_α. We show the T dependence of τ_χ along with τ_α

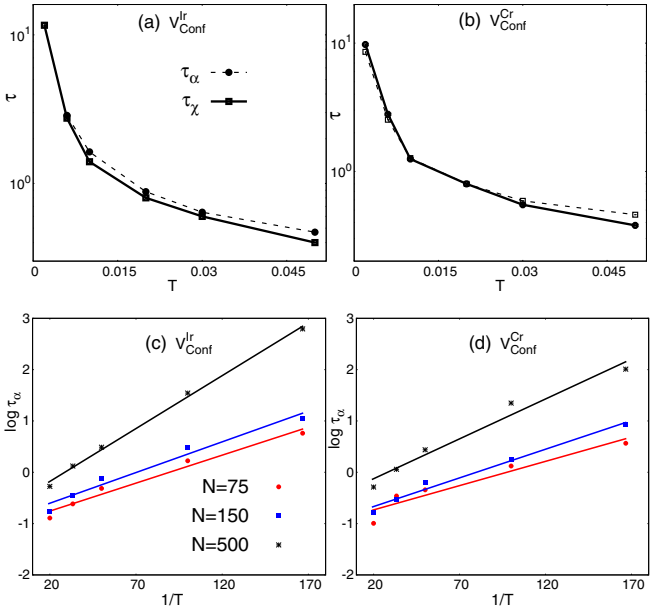

FIG. 13. T dependence of τ_χ along with τ_α, obtained from $Q(t)$ for irregular (a) and circular (b) confinements, respectively, with $N = 150$. Both the time scales show similar T dependences. The T-dependence of τ_α for different N is shown in panel c,d for irregular and circular confinements, respectively. The solid line shows the exponential fitting ($\tau_\alpha \propto \exp[-A/T]$) to the actual data (points).

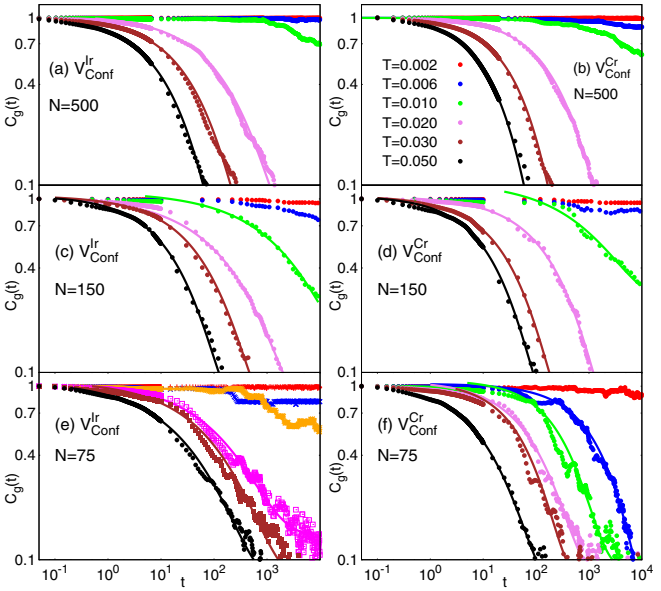

FIG. 14. Decay of cage correlation function, $c_g(t)$, depicting how the initial neighbors fail, with time, to confine a particle, on average, at different T for $N = 500$ [panels (a), (b)], 150 [panels (c), (d)], and 75 [panels (e), (f)] for irregular and circular confinements, respectively. The solidity at low T is reflected in the fact that the same neighbors continue to cage a particle at all times. The solid line shows the best fit to the actual data (points).

in Figs. 13(a) and 13(b) for V^{Ir}_{conf} and V^{Cr}_{conf}, respectively, with $N = 150$. For both the confinements, the T dependences of these two characteristic times are essentially identical within the tolerance. The rapid increase of τ_χ and τ_α with decrease in T are reminiscent of glassy systems. Since, for any given N, T dependences of τ_χ and τ_α are similar, in Figs. 13(c) and 13(d) we show the dependence of τ_α on T for different N. We find that $\tau_\alpha \propto \exp[-A/T]$ [80] for any given N and A shows a weak dependence on N (for details, see Appendix H).

2. *Cage-correlation time*

The role of repulsive interparticle interaction on the physical properties of Coulomb clusters can be further probed by addressing the cage effects, in which each particle is locked up by its neighbors. Rearrangement of cage due to thermal fluctuations relaxes the system and thereby the particles diffuse in the system. The rate of change of neighbors of a particle yields a cage correlation function (CCF) and helps in understanding how rapidly the local environment of each particle changes on an average. We note here that in glass formers, too, particle motion gets slower, without appreciable change in the structure, upon approaching the glass transition temperature.

We calculate CCF by first defining a neighbor list, keeping track of the neighbors of each particle. A neighbor list $\mathbf{L^{(i)}(t)}$ for particle i in an N particle system is a vector of length N and is defined as [82] $\mathbf{L^{(i)}_j(t)} = 1$ if j is the nearest neighbor of i at time t and zero otherwise, with $j = 1,2,\ldots,N$. We use the Voronoi construction [67] to select neighbor list at all t.

The CCF at t is given by

$$C_g(t) = \frac{\langle \mathbf{L_i(t)} \cdot \mathbf{L_i(0)} \rangle}{\langle \mathbf{L_i^2(0)} \rangle}. \tag{12}$$

If all the neighbors of the particle at time t is identical to the list at time $t = 0$, CCF assumes unity for that particle. If, however, all the neighbors of a particle gets changed, CCF becomes zero at that instant of time.

In Figs. 14(a) and 14(b), we show the decay of CCF at different T for irregular and circular confinements, respectively, with $N = 500$. For both the confinements, $C_g(t)$ remains close to unity for all times at $T \leqslant 0.006$, implying no significant rearrangements of neighbors. As T increases, $C_g(t)$ shows a decay in both the confinements of following form: $c_g(t) \propto \exp[-(t/\tau_g)^\beta]$ with $\beta < 1$ [80]. The exponent β is found smaller for V^{Ir}_{conf} compared to that of V^{Cr}_{conf}, as illustrated in Appendix I.

The t dependence of $c_g(t)$ for different T with $N = 150$ is shown in Figs. 14(c) and 14(d) for V^{Ir}_{conf} and V^{Cr}_{conf}, respectively. While $c_g(t)$ stays close to unity for $T = 0.002$, note that with a decrease in N, $C_g(t)$ decays more rapidly for both the confinements while the decay is faster for V^{Cr}_{conf} compared to V^{Ir}_{conf}. Particularly, for $N = 75$, $C_g(t)$ decays quite rapidly for V^{Cr}_{conf} [Fig. 14(f)] at $T = 0.010$. Thus, compared to V^{Ir}_{conf} [Fig. 14(e)], the local rearrangement occurs more frequently for smaller N in V^{Cr}_{conf}, which in turn causes the bond orientational order to deplete rapidly, as reflected in $g_6(t)$ and ψ_6.

We find that for different N, the exponent remains in the range $0.45 \leqslant \beta \leqslant 0.7$ (see Appendix I). Recently, it was found that $C_g(t)$ for supercooled liquids [83] and for water in nanoporous silica [84] show stretched exponential

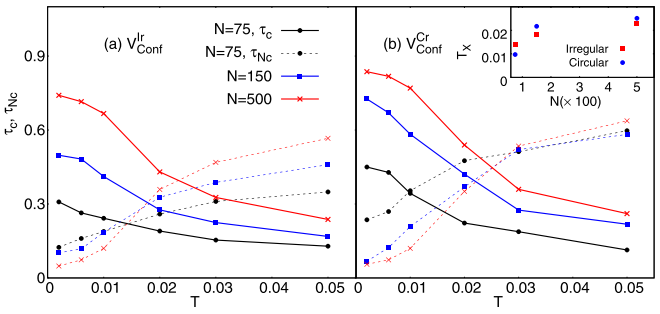

FIG. 15. T dependence of average caging (τ_C) and noncaging (τ_{NC}) times for different N for irregular (a) and circular (b) confinements. Crossover temperature T_X is estimated from the crossing of τ_C and τ_{NC}. Inset in panel (b) shows the N dependence of the estimated T_X for both the confinements.

decay with the characteristics exponent $\beta = 0.6$. In fact, a stretched exponential temporal decay is very common to supercooled liquids [85]. For a system with static random traps, the asymptotic value of β relates the dimensionality d of the system through $\beta = d/(d+2)$ [86]. Thus, for $d = 2$, asymptotic value of β is 0.5. Our results are in broad agreement with such prediction and experiments.

We can also probe the time scale associated with local rearrangements of particles by studying the relative fluctuations in position of the particles with respect to its neighbors. A perfectly caged particle is expected to have equidistant neighbors. Exploiting this idea, we define the caging time (τ_C) of the ith particle as the time up to which the following condition holds for at least three of its neighboring particles (j):

$$\frac{\sigma_i(t)}{\Delta r_{ij}(t)} \leqslant d; \quad \text{for at least } j = 3.$$

Here $j = 1,2,\ldots,N_b$, with N_b denoting the number of nearest neighbors of particle i; $\Delta r_{ij}(t) = |\vec{r}_i(t) - \vec{r}_j(t)|$ and $\sigma_i^2(t) = \langle \Delta^2 r_{ij}(t)\rangle - \langle \Delta r_{ij}(t)\rangle^2$. We take cutoff value d/r_0 as 0.1, analogous to the usual Lindemann ratio. Once the above criterion breaks down, then the time taken by the particle to get caged again is called the noncaging time (τ_{NC}). In the above, caging is defined at least with respect to three of its neighbors, because in 2D a minimum of three particles are required to cage a particle. Figures 15(a) and 15(b) show the average τ_C and τ_{NC} for irregular and circular confinements, respectively, for different N. Here, τ_C and τ_{NC} are expressed relative to the total time of the MD simulation. At low T, caging time is expectedly high as particles are mostly confined by its nearest neighbors. As T increases, thermal energy overcomes caging. Thus, average τ_C decreases and consequently τ_{NC} increases with increase in T. We find that, for a given N, average τ_C and τ_{NC} cross each other around $T \sim T_X$ for both the confinements [see inset of Fig. 15(b)]. Note that this analysis of τ_C and τ_{NC} excludes the particles on the boundary because the definition of caging does not work for them.

3. *Persistence and exchange time*

A crucial time scale that probes the dynamic heterogeneity as well as glassiness is the contrasting behavior of the persistence and exchange times [87,88]. They are defined as

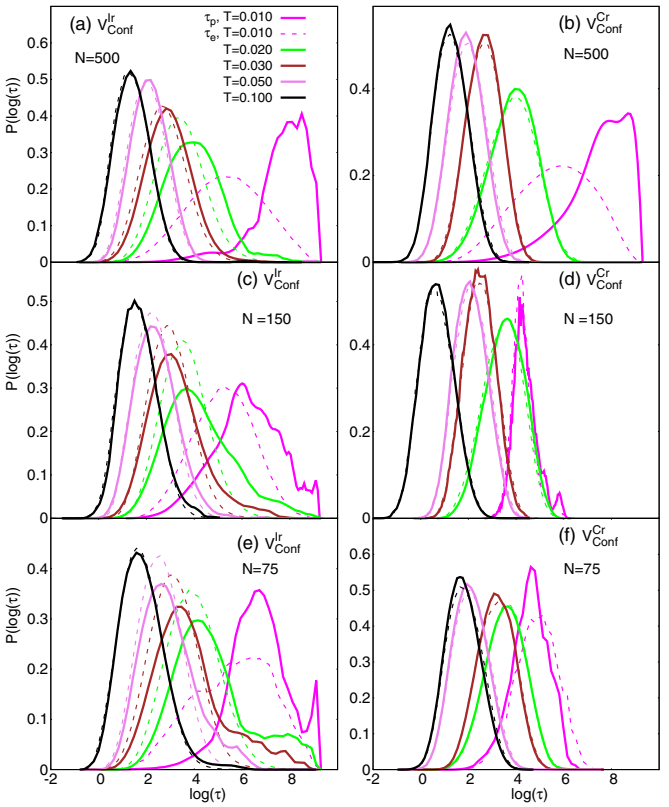

FIG. 16. Distribution of persistence (τ_p) and exchange (τ_e) times for $N = 500$ [panels (a), (b)], $N = 150$ [panels (c), (d)], and $N = 75$ [panels (e), (f)] particles in irregular and circular confinements, respectively. In the figure all quantities are expressed as log to the base e. The decoupling of the two distributions at low T demonstrates the qualitative similarity of the particle dynamics in irregular traps with those in glassy systems. Such decoupling is hard to discern (except for $T = 0.010$) for circular traps for all N.

follows: At any given T, let us consider a particle i, whose initial ($t = 0$) position is $r_i(0)$. The persistence time t_1 for a given cutoff distance r_p is specified by the first time that particle i has moved far enough that $|r_i(t_1) - r_i(0)| \geqslant r_p$.

Exchange times $t_n - t_{n-1}$ for $n > 1$ require the recursive determination t_n, setting t_{n-1} as initial time. For a given r_p, distributions of exchange (τ_e) and persistence (τ_p) times can be obtained by ensemble averaging over all trajectories. r_p is chosen of the order of r_0 so as to probe the structural relaxation and diffusion. The same r_p is used for all T. It has been shown [87,88] that for glassy dynamics, distribution of (τ_e) and (τ_p) generally decouple near the glass transition temperature. This decoupling is attributed to dynamic heterogeneity in these systems and constitutes one of the key features of supercooled liquids [87,88].

The distributions of these two time scales for our clusters are shown in Fig. 16 for irregular [Fig. 16(a)] and circular [Fig. 16(b)] confinements with $N = 500$. We notice that for $T > 0.030$, $P(\tau_e)$ and $P(\tau_p)$ coincide for both the confinements. As T becomes close to $T_X(\approx 0.020)$, the two distributions become distinct; the mean value for $P(\tau_p)$ moves toward longer times for IWM. But for circular confinement, $P(\tau_e)$ and $P(\tau_p)$ coincide even at $T = 0.020$. Thus, the

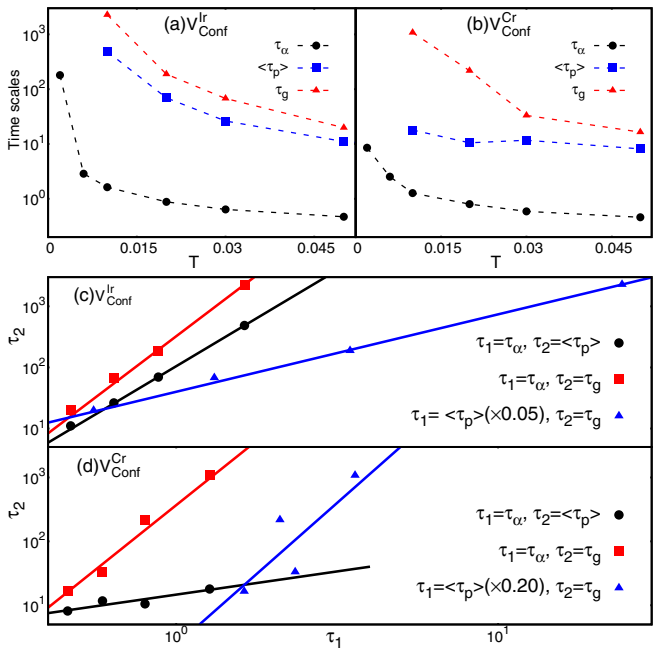

FIG. 17. T dependence of structural relaxation time τ_α, average persistence time $\langle\tau_p\rangle$, and cage correlation time τ_g for (a) irregular and (b) circular confinements with $N = 150$. Dotted lines are for visual guidance. Panels (c) and (d): Thick dots show the cross-correlation between $\tau_\alpha, \langle\tau_p\rangle$, and τ_g in a log-log plot for irregular and circular confinement, respectively, taken over a temperature range $0.01 \leqslant T \leqslant 0.05$. Solid lines represent the best fit to such correlations. $\langle\tau_p\rangle$ is scaled by appropriate factors for visual clarity.

distribution of τ_p and exchange τ_e gets decoupled for irregular confinement as system approaches T_X. Below T_X, we find that $P(\tau_e)$ and $P(\tau_p)$ decouple even for circular confinement. Does such decoupling occur even for smaller N? Figures 16(c) and 16(d) show T dependence of $P(\tau_e)$ and $P(\tau_p)$ for $N = 150$ and Figs. 16(e) and 16(f) show it for $N = 75$ particles in irregular and circular confinements, respectively. We find that such decoupling of the two time scales also occurs for $N = 150$ [Fig. 16(c)] and 75 [Fig. 16(e)] particles in irregular confinement. The decoupling is more prominent in irregular than circular confinement. For CWM, decoupling, if there is any, is present only for very low $T(\leqslant 0.010)$. We have ensured that the decoupling is not because of bias in the sampling process by carrying out the jackknife test [89] and Ansari-Bradley [90] test.

Since the overlap function, cage correlation function, and persistence time all are connected with the structural relaxation of the system, we now look into the T dependence of the characteristic time scales associated with all these quantities. For example, cage correlation time τ_g represents the characteristic time scale for the rearrangement of particles in their local environment and average persistence time $\langle\tau_p\rangle$ depicts the time required for particles to move a certain distance on average and thus is associated with the relaxation mechanism in the system. In Fig. 17, we show the T dependence of τ_α, τ_g, and $\langle\tau_p\rangle$ for irregular [Fig. 17(a)] and circular confinements [Fig. 17(b)] with $N = 150$. We find that all these time scales increase rapidly for the IWM compared to CWM as T is decreased below T_X. Thus, the signatures of glassy dynamics, while showing up in both confinements, are more prominent for irregular confinement.

4. *Cross-correlation between different relaxation times*

Here, we study the cross-correlation between the different time scales described above. Figure 17(c) illustrates the cross-correlations between τ_α and τ_g, τ_α and $\langle\tau_p\rangle$, and $\langle\tau_p\rangle$ and τ_g, gathered over a temperature window across melting; namely, $0.01 \leqslant T \leqslant 0.05$, for irregular confinement. Our results indicate that there is a positive correlation between these characteristic times scales; when one goes up, the other increases too, in a proportionate manner. Quantifying such correlations, we find that $\tau_i \propto \tau_j^{c_{ij}}$ [80] with the following sets of best-fit parameters $\{\tau_i, \tau_j, c_{ij}\}$: $\{\tau_\alpha, \tau_p, 3.14\}$, $\{\tau_\alpha, \tau_g, 3.98\}$, and $\{\tau_p, \tau_g, 1.27\}$. Similar positive correlation between different times scales is also observed for circular confinement as depicted in Fig. 17(d). In this case, we find $\{\tau_i, \tau_j, c_{ij}\}$: $\{\tau_\alpha, \tau_p, 0.73\}$, $\{\tau_\alpha, \tau_g, 4.03\}$, and $\{\tau_p, \tau_g, 4.45\}$. Thus, all these time scales help in characterizing the multiscale relaxation in our Coulomb clusters.

V. CONCLUSIONS

In conclusion, we have carried out a comprehensive simulation of static and dynamic properties to understand the thermal crossover of Coulomb interacting particles in traps. Our results offer insights into the possibility of observing intriguing phases in confined 2D systems. Signatures of hexatic-like phases for Coulomb clusters are discerned from their healthy bond orientational order at low temperatures, as seen from the distribution of ψ_6 and its projection on the mean local orientational order, ϕ_6. This assertion is further strengthened from the temporal bond orientation correlation function, $g_6(t)$, showing an algebraic decay for a window of temperatures. Expectedly, we find the lack of positional order in irregular Wigner molecules. Circular Wigner molecules, however, show competition of triangular lattice-like positional ordering in the central portion of the trap whereas the regions near the boundary follow circular symmetry. Thus, at least for the irregular (hence, disordered) systems, any rigidity of the solid-like phase is quantified through the strength of the bond orientational order. Consequently, melting in a Coulomb cluster is identified through the breakdown of this bond orientational rigidity.

We find that it is difficult to observe generic trends for systems with small $N(< 75)$ and their behavior shows special features because of the larger boundary-to-bulk particle ratios for those N's. In particular, we find that circular Wigner molecule with small N undergoes crossover at lower temperature as seen from, e.g., generalized susceptibilities, fraction of solid- and liquid-like particles, and caging and noncaging time. We analyzed several melting criteria, often taking advantage of the confined geometries, all of which point toward a unique crossover temperature (within tolerance) for $N > 100$. When this crossover temperature is expressed in terms of dimensionless coupling Γ (defined in Sec. III C), we get $\Gamma_c \approx 147$ for $N > 100$, which is close to the predicted critical value, $\Gamma_c \approx 137$, for the bulk 2D systems.

While static responses are qualitatively similar for irregular and circular confinements, dynamical correlations yield distinct signatures. With decreasing temperature, dynamics of particles become slow and strongly heterogeneous due to caging effects in irregular trap though the bond orientational order gets strengthened in both circular and irregular geometries. We find a stretched exponential decay of spatial correlations in irregular confinement. Instead, a stretched Gaussian behavior identifies circular traps, which is also observed experimentally [75,76]. We also witness some of the key signatures of glassy dynamics in Coulomb clusters, such as spatially correlated motion of particles over longer distances forming a tortuous string-like paths, stretched exponential decay of correlations, strong increase of relaxation times with lowering temperature, and decoupling of persistence and exchange times for $T \leqslant T_X$. All these indicate that a hexatic-like phase with features of glassy dynamics is realized in finite systems, at least in those with disorder and long-range interactions. Note that the glassy behavior that we observe for Coulomb clusters are usually found in literature only for systems with short-range interactions [49,56,87] (spin glasses, however, are realized with long-range interactions [91]). A hexatic-glass phase, differing from the usual hexatic phase in 2D only by its quenched randomness, makes the study of defects in our system an interesting proposition. We hope that our results will help enrich the knowledge of melting in two-dimensional confinements.

ACKNOWLEDGMENTS

The authors thank Chandan Dasgupta for valuable discussions. We acknowledge computational facilities at IISER Kolkata. B.A. acknowledges the University Grant Commission (UGC), India, for a doctoral fellowship. A.G. acknowledges the hospitality of the Aspen Center for Physics and was supported in part by the Simons Foundation.

APPENDIX A: CHOICE OF THE SPATIAL EXTENT OF THE CENTRAL REGION TO EVALUATE $\rho(\vec{k})$

In order to justify our choice for the region inside the system, we have looked into the radial distribution, $n(r)$, of the $N = 500$ particles in circular confinements at the lowest $T(= 0.002)$. Here, the distance r is measured from the center of the confining potential and in units of average interparticle distance, r_0. Figure 18(a) shows that only for $r > R_c = 9.3$ [indicated by dashed line in Fig. 18(a)], there are well-separated peaks in $n(r)$, implying that the outer shells have a well-defined radius. Because of the formation of a triangular lattice-like structure, the distribution $n(r)$ does not have well-separated peaks for small r. This fact can also be identified by looking into the bond orientational order (BOO) by considering the particles for which $r < R_c$ (bulk particles) and those for which $r > R_c$ (boundary particles), as shown in Fig. 18(b). Here, we can see that distribution is sharply peaked around 1 for bulk particles compared to that for particles on the outer shells, confirming the formation of hexagonal ordered structure in the bulk for circular confinement with $N = 500$ particles. This choice of R_c restricts the maximum possible length along the X axis to be $l_x \sim 7r_0$ and along the Y axis

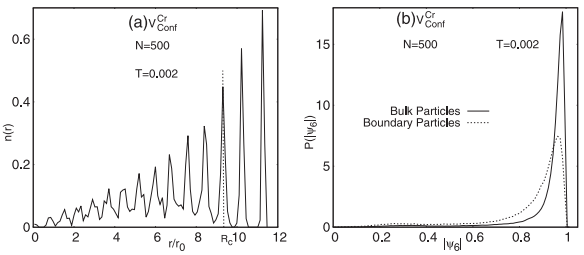

FIG. 18. (a) Radial distribution, $n(r)$, of the $N = 500$ particles in circular confinement at $T = 0.002$. The dashed line shows the cutoff distance R_c used to identify the bulk particles. (b) Distribution of the bond orientational order ψ_6 for particles having r (distance from the center of the confinement) $< R_c$ (bulk particles; solid line) and those for which $r > R_c$ (boundary particles; dashed line) in circular confinement at $T = 0.002$.

to be $l_y = \sqrt{3}l_x/2$ (to consider a commensurate triangular lattice), as we must have

$$\begin{aligned} l_x^2 + l_y^2 &< R_c^2, \\ l_x^2 + \left(\frac{\sqrt{3}}{2}l_x\right)^2 &< (9.3)^2, \\ \frac{7l_x^2}{4} &< (9.3)^2, \\ l_x &< 7.03. \end{aligned} \tag{A1}$$

Once we have chosen the small region for circular confinement, the same length scales were used for irregular confinement to investigate the effect of disorder in the system.

APPENDIX B: Γ VALUES FOR CIRCULAR AND IRREGULAR CONFINEMENTS

In the main article, we have mentioned the value of the parameter Γ at the crossover temperature. Here, in Table II, we have tabulated Γ values for all T and N for irregular and circular confinements.

APPENDIX C: COMPARISON OF t DEPENDENCE OF $g_6(t)$ FOR DIFFERENT N

In Fig. 19, we show the t dependence of $g_6(t)$ for different N at $T = 0.006$ [Figs. 19(a) and 19(b)], $T = 0.020$ [Figs. 19(c) and 19(d)], and $T = 0.050$ [Figs. 19(e) and 19(f)] for irregular and circular confinements, respectively. At $T = 0.006$, with decreasing N, $g_6(t)$ starts to decay slowly at long time for irregular confinement [Fig. 19(a)] while it decays quite rapidly for circular confinement [Fig. 19(b)]. Such rapid breakdown of orientational order at low T for $N = 75$ in $V_{\text{Conf}}^{\text{Cr}}$ indicates the fact that crossover temperature, T_X (as computed from the fluctuation of bond orientational order discussed in main article), is lower for $N = 75$. At intermediate $T(= 0.020)$, $g_6(t)$ shows algebraic decay for all N [Figs. 19(c) and 19(d)] and for both the confinements. For circular confinement with $N = 75$ [Fig. 19(d)], $g_6(t)$ first decays exponentially and then fluctuates around some mean value. At $T = 0.050$, $g_6(t)$ shows exponential decay for all N in both the confinements.

TABLE II. Estimation of the parameter $\Gamma = \sqrt{\pi n}/T$, characterizes the melting in bulk 2D systems, for irregular and circular confinements. For bulk systems $\Gamma \approx 137$ at the transition. Note that the average particle density n is estimated by computing the area covered by N particles in the respective confinements.

		Irregular confinement			Circular confinement		
N	T	n	$a = \sqrt{n\pi}$	$\Gamma = a/T$	n	$a = \sqrt{n\pi}$	$\Gamma = a/T$
500	0.002	3.01	3.075	1537.5	2.78	2.955	1477.5
	0.006			512.5			492.5
	0.010			307.5			295.5
	0.015			205.0			197.5
	0.020			153.8			147.8
	0.025			123.0			118.2
	0.030			102.5			98.5
	0.050			61.5			59.1
150	0.002	2.53	2.819	1409.5	2.12	2.581	1209.5
	0.006			469.8			430.2
	0.010			281.9			258.1
	0.015			187.9			172.1
	0.020			140.9			129.1
	0.025			112.8			103.2
	0.030			93.9			86.0
	0.050			56.4			51.6
75	0.002	2.42	2.757	1378.5	1.90	2.44	1220.0
	0.006			459.5			406.7
	0.010			275.7			244.0
	0.015			183.8			162.7
	0.020			137.8			122.0
	0.025			110.3			97.6
	0.030			91.9			81.3
	0.050			55.1			48.8

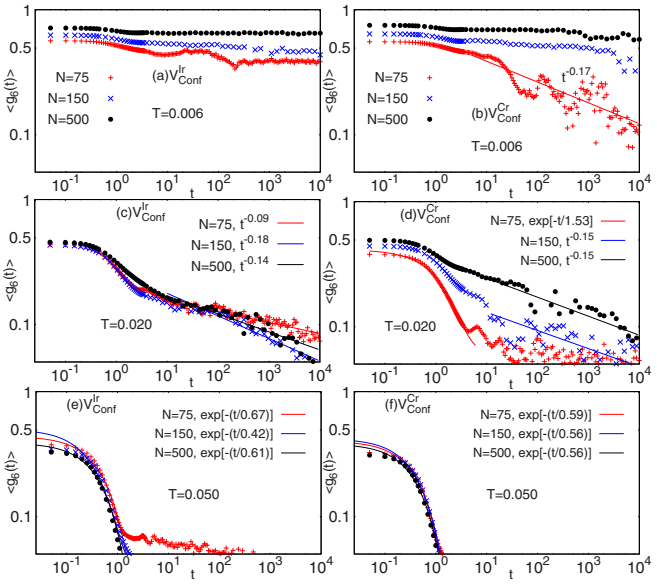

FIG. 19. t dependence of exponent $g_6(t)$ for different N at $T = 0.006$ [panels (a) and (b)], $T = 0.020$ [panels (c) and (d)], and $T = 0.050$ [panels (e) and (f)] for irregular and circular confinements, respectively. Points represent the actual data while the solid line represents an appropriate fit of the selected data (determined by the extent of the solid line).

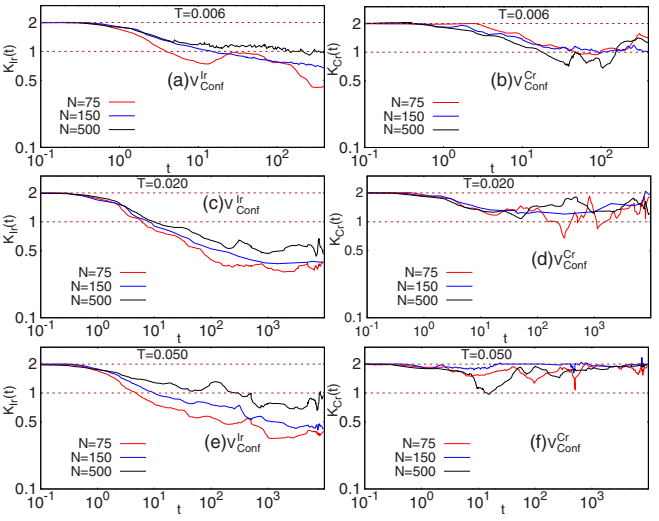

FIG. 20. t dependence of exponent $k(t)$ for different N at $T = 0.006$ [panels (a), (b)], $T = 0.020$ [panels (c), (d)], and $T = 0.050$ [panels (e), (f)] for irregular ($k_{\rm Ir}$) and circular ($k_{\rm Cr}$) confinements, respectively.

APPENDIX D: COMPARISON OF TIME EVOLUTION OF EXPONENT $k(t)$ FOR DIFFERENT N

In Fig. 20, we show the time evolution of the exponent $k_{\rm Ir}$ and $k_{\rm Cr}$ (see the main text for details), respectively, for different N at $T = 0.006$ [Figs. 20(a) and 20(b)], $T = 0.020$ [Figs. 20(c) and 20(d)], and $T = 0.050$ [Figs. 20(e) and 20(f)]. For all these T, we find that the $k_{\rm Ir}$ attains lower value, on an average, with decrease in N, implying that effect of disorder is more prominent for small N. For $k_{\rm Cr}$, the long-time behavior is similar for all N and T.

APPENDIX E: CHOICE OF CUTOFF DISTANCE r_c FOR OVERLAP FUNCTION $Q(t)$

$Q(t)$ depends on the choice of r_c and the optimal r_c is chosen as follows: We study the fluctuation of $Q(t)$, defined as the dynamical susceptibility

$$\chi_4(t) = \frac{1}{N}[\langle Q^2(t)\rangle - \langle Q(t)\rangle^2] \tag{E1}$$

at low T for different choices of r_c. From the definition, we see that $\chi_4(t) = 0$ when no particle moves by a distance beyond r_c. It is zero, as well, when displacements of all the particles are greater than r_c. So there must be a time scale, τ_χ, when $\chi_4(\tau_\chi)$ reaches maximum for a given r_c. Thus, the maximum of χ_4, i.e., the fluctuations in $Q(t)$, at $t = \tau_\chi$ signifies the maximal dynamic heterogeneity. At a given T, we choose the value of r_c for which such dynamic heterogeneity attains the maximum. For each N, we have done this analysis for irregular confinement and use the same r_c for circular confinement. For example, we find that for $N = 150$, $\chi_4(t)$ reaches its maximum for $r_c = 0.09$ (Fig. 21), which is about 14% of r_0. Once r_c is chosen, then we study the t dependence of overlap function $Q(t)$ and $\chi_4(t)$ for different N. Similar analyses for $N = 500$ and 75 yield $r_c = 0.12$ and 0.08, respectively.

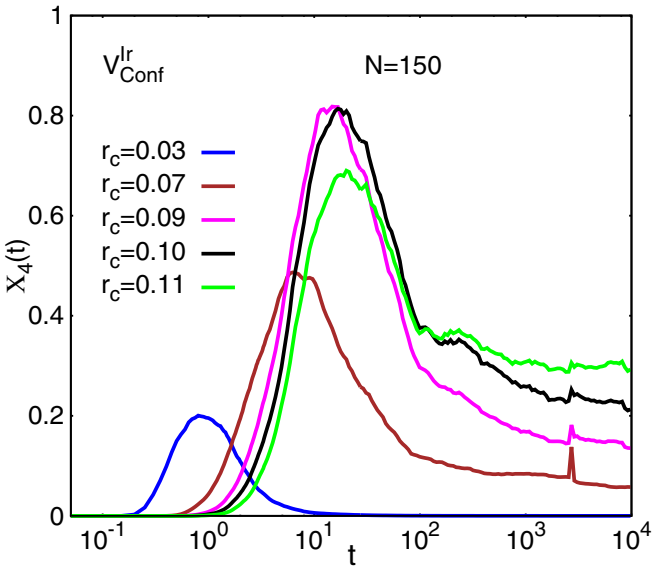

FIG. 21. Determination of the cutoff r_c for $V^{\rm Ir}_{\rm conf}$ with $N = 150$, by tracking its value for which $\chi_4(t)$ achieves the maximum keeping temperature fixed at its lowest value ($T = 0.002$). This optimal $r_c = 0.09$ is then used for the evaluation of the overlap function $Q(t)$.

APPENDIX F: DETAILS OF THE FITTING PARAMETERS FOR OVERLAP FUNCTION

Beyond a very short time, the time dependence of overlap function $Q(t)$ can be expressed as $Q(t) \propto \exp[-(t/\tau_\alpha)^c]$. For a given N, the details of the fitting parameters τ_α and c for both the confinements at different T are given in Table III. We find that for irregular confinement $Q(t)$ decays exponentially ($c = 1$) for $T > 0.01$ for all N, whereas it is stretched exponentially ($c < 1$) for lower T and has a much slower decay for $T = 0.002$. For circular confinement, $Q(t)$ shows predominantly an exponential decay, while stretched exponential decay is found for $N \geqslant 150$ at very low T.

TABLE III. Details of the fitting parameters, τ_α and c, of the overlap function function, $Q(t)$, for irregular and circular confinements.

		Irregular confinement		Circular confinement	
N	T	τ_α	c	τ_α	c
500	0.006	5.96	0.34	6.51	0.57
	0.010	4.19	0.72	3.81	1.00
	0.020	1.36	1.00	1.22	1.00
	0.030	0.86	1.00	0.77	1.00
	0.050	0.59	1.00	0.55	1.00
150	0.002			8.24	0.73
	0.006	2.75	0.82	2.13	1.00
	0.010	1.62	1.00	0.94	1.00
	0.020	0.64	1.00	0.58	1.00
	0.030	0.47	1.00	0.42	1.00
	0.050	0.34	1.00	0.33	1.00
75	0.006	1.82	0.76	1.39	1.00
	0.010	1.63	1.00	0.84	1.00
	0.020	0.54	1.00	0.50	1.00
	0.030	0.40	1.00	0.45	1.00
	0.050	0.31	1.00	0.28	1.00

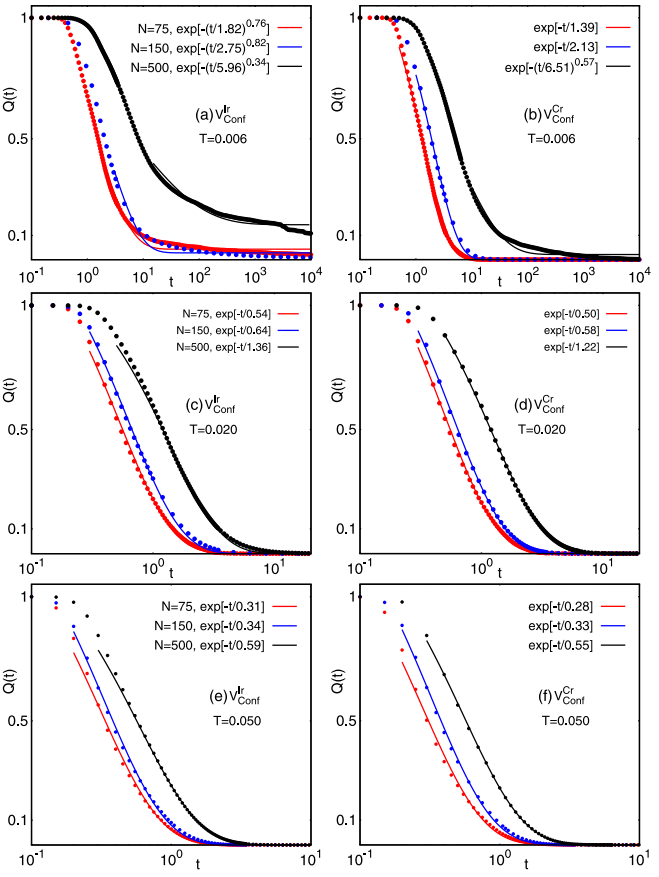

FIG. 22. t dependence of exponent $Q(t)$ for different N at $T = 0.006$ [panels (a), (b)], $T = 0.020$ [panels (c), (d)], and $T = 0.050$ [panels (e), (f)] for irregular and circular confinements, respectively.

APPENDIX G: t DEPENDENCE OF $Q(t)$ FOR DIFFERENT N

Figure 22 shows the N dependence of $Q(t)$ for $T = 0.006$ [Figs. 22(a) and 22(b)], $T = 0.020$ [Figs. 22(c) and 22(d)], and $T = 0.050$ [Figs. 22(e) and 22(f)] for irregular and circular confinements, respectively. At all T, the characteristic time scale τ_α increases with N. At $T = 0.006$, while $Q(t)$ shows stretched exponential decay for irregular confinement [Fig. 22(a)], it is exponential for circular confinement with $N \leqslant 150$ [Fig. 22(b)]. For $N = 500$, we find stretched exponential decay even for circular confinement. $Q(t)$

TABLE IV. Dependence of the fitting parameter, A, for structural relaxation time, τ_α, on particle number N for irregular and circular confinements.

N	Irregular confinement	Circular confinement
	A	A
500	0.021	0.016
150	0.012	0.011
75	0.011	0.009

TABLE V. Details of the fitting parameters, τ_g and β, of the cage correlation function, $c_g(t)$, for circular and irregular confinements. For both the confinements, the decay of $c_g(t)$ is stretched exponentially, $\beta < 1$.

		Irregular confinement		Circular confinement	
N	T	τ_g	β	τ_g	β
500	0.020	202.60	0.56	242.78	0.62
	0.030	52.86	0.60	43.87	0.69
	0.050	19.30	0.63	15.66	0.68
150	0.010	2271.83	0.45	1077.54	0.48
	0.020	188.00	0.44	216.93	0.58
	0.030	67.69	0.55	33.18	0.61
	0.050	19.82	0.60	16.47	0.63
75	0.006			1734.08	0.70
	0.010			356.41	0.73
	0.020	152.14	0.48	96.69	0.63
	0.030	108.00	0.48	63.51	0.72
	0.050	34.49	0.45	12.75	0.57

decays exponentially for both the confinements for $T \geqslant 0.02$ [Figs. 22(c)–22(f)].

APPENDIX H: DETAILS OF THE FITTING PARAMETERS FOR STRUCTURAL RELAXATION TIME, τ_α

In the main text, we discussed that the structural relaxation time, τ_α, computed from the overlap function, $Q(t)$, shows following functional dependency on T for any given N: $\tau_\alpha \propto \exp[-A/T]$. Table IV shows the fitting parameter A for different N for irregular and circular confinements.

APPENDIX I: DETAILS OF THE FITTING PARAMETERS FOR CAGE CORRELATION FUNCTION

The cage correlation function, $c_g(t)$, is fitted with the following functional form:

$$c_g(t) \propto \exp\left[-\left(\frac{t}{\tau_g}\right)^{\beta}\right].$$

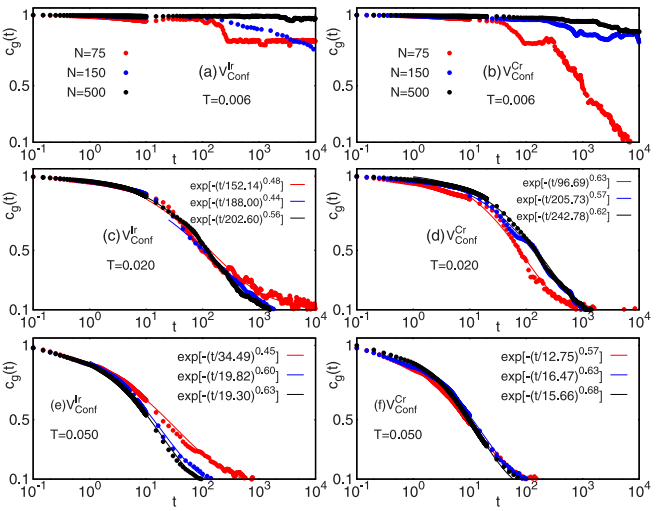

FIG. 23. t dependence of exponent $c_g(t)$ for different N at $T = 0.006$ [panels (a) and (b)], $T = 0.020$ [panel (c) and (d)], and $T = 0.050$ [panels (e) and (f)] for irregular and circular confinements, respectively.

For both the confinements, $c_g(t)$ shows stretched exponential decay ($\beta < 1$) and values of τ_g and β at different T is given in Table. V. Here, we find that τ_g, the characteristic time scale associated with the local rearrangement of particles, grows more rapidly with decrease in T, for irregular confinement, reinstating the glassy dynamics in $V^{\rm Ir}_{\rm conf}$.

APPENDIX J: t DEPENDENCE OF $C_g(t)$ FOR DIFFERENT N

Figure 23 shows the N dependence of $c_g(t)$ for $T = 0.006$ [Figs. 23(a) and 23(b)], $T = 0.020$ [Figs. 23(c) and 23(d)], and $T = 0.050$ [Figs. 23(e) and 23(f)] for irregular and circular confinements, respectively. Like overlap function $Q(t)$, the characteristic time scale τ_g also increases with N. Note that for circular confinement $c_g(t)$ decays quite rapidly at $T = 0.006$ for $N = 75$, implying significant local rearrangement of particles for smaller N. This is also similar to what is observed for $g_6(t)$.

[1] E. M. Chudnovsky, Phys. Rev. B **40**, 11355 (1989).
[2] J. M. Kosterlitz and D. J. Thouless, J. Phys. C: Solid State Phys. **5**, L124 (1972).
[3] J. M. Kosterlitz and D. J. Thouless, J. Phys. C: Solid State Phys. **6**, 1181 (1973).
[4] B. I. Halperin and D. R. Nelson, Phys. Rev. Lett. **41**, 121 (1978).
[5] D. R. Nelson and B. I. Halperin, Phys. Rev. B **19**, 2457 (1979).
[6] A. P. Young, Phys. Rev. B **19**, 1855 (1979).
[7] R. E. Kusner, J. A. Mann, and A. J. Dahm, Phys. Rev. B **49**, 9190 (1994).
[8] A. Zippelius, B. I. Halperin, and D. R. Nelson, Phys. Rev. B **22**, 2514 (1980).
[9] R. Seshadri and R. M. Westervelt, Phys. Rev. Lett. **66**, 2774 (1991).
[10] J. Toner, Phys. Rev. Lett. **66**, 2523 (1991).
[11] E. M. Chudnovsky, Phys. Rev. Lett. **67**, 1809 (1991).
[12] J. Toner, Phys. Rev. Lett. **67**, 1810 (1991).
[13] S. T. Chui and B. Tanatar, Phys. Rev. Lett. **74**, 458 (1995).
[14] L. Kouwenhoven and C. Marcus, Phys. World **11**, 35 (1998).
[15] E. Wigner, Phys. Rev. **46**, 1002 (1934).
[16] J. Böning, A. Filinov, P. Ludwig, H. Baumgartner, M. Bonitz, and Y. E. Lozovik, Phys. Rev. Lett. **100**, 113401 (2008).
[17] R. Egger, W. Häusler, C. H. Mak, and H. Grabert, Phys. Rev. Lett. **82**, 3320 (1999).
[18] V. M. Bedanov and F. M. Peeters, Phys. Rev. B **49**, 2667 (1994).
[19] D. Bhattacharya and A. Ghosal, Eur. Phys. J. B **86**, 499 (2013).
[20] D. Bhattacharya, A. V. Filinov, A. Ghosal, and M. Bonitz, Eur. Phys. J. B **89**, 60 (2016).

[21] B. Ash, J. Chakrabarti, and A. Ghosal, Europhys. Lett. **114**, 46001 (2016).
[22] M. Kong, B. Partoens, and F. M. Peeters, New J. Phys. **5**, 23 (2003).
[23] S. W. S. Apolinario, B. Partoens, and F. M. Peeters, Phys. Rev. E **72**, 046122 (2005).
[24] M. Girotto, A. P. dos Santos, T. Colla, and Y. Levin, J. Chem. Phys. **141**, 014106 (2014).
[25] R. Bubeck, C. Bechinger, S. Neser, and P. Leiderer, Phys. Rev. Lett. **82**, 3364 (1999).
[26] L. Q. Costa Campos, S. W. S. Apolinario, and H. Löwen, Phys. Rev. E **88**, 042313 (2013).
[27] M. Golosovsky, Y. Saado, and D. Davidov, Phys. Rev. E **65**, 061405 (2002).
[28] A. Melzer, A. Schella, T. Miksch, J. Schablinkski, D. Block, A. Piel, H. Thomsen, H. Khlert, and M. Bonitz, Contrib. Plasma Phys. **52**, 795 (2012).
[29] H. Thomsen, H. Khlert, M. Bonitz, J. Schablinski, D. Block, A. Piel, and A. Melzer, Phys. Plasmas **19**, 023701 (2012).
[30] J. H. Chu and I. Lin, Phys. Rev. Lett. **72**, 4009 (1994).
[31] R. C. Ashoori, Nature (London) **379**, 413 (1996).
[32] L. P. Kouwenhoven, D. G. Austing, and S. Tarucha, Rep. Prog. Phys. **64**, 701 (2001).
[33] I. M. Buluta and S. Hasegawa, J. Phys. B: At., Mol. Opt. Phys. **42**, 154004 (2009).
[34] C. C. Grimes and G. Adams, Phys. Rev. Lett. **42**, 795 (1979).
[35] S. Mahmoudian, L. Rademaker, A. Ralko, S. Fratini, and V. Dobrosavljević, Phys. Rev. Lett. **115**, 025701 (2015).
[36] L. Rademaker, Y. Pramudya, J. Zaanen, and V. Dobrosavljević, Phys. Rev. E **88**, 032121 (2013).
[37] N. D. Mermin and H. Wagner, Phys. Rev. Lett. **17**, 1133 (1966).
[38] Y. Han, N. Y. Ha, A. M. Alsayed, and A. G. Yodh, Phys. Rev. E **77**, 041406 (2008).
[39] H. H. von Grünberg, P. Keim, K. Zahn, and G. Maret, Phys. Rev. Lett. **93**, 255703 (2004).
[40] Y. Peng, Z. Wang, A. M. Alsayed, A. G. Yodh, and Y. Han, Phys. Rev. Lett. **104**, 205703 (2010).
[41] S. Prestipino, F. Saija, and P. V. Giaquinta, Phys. Rev. Lett. **106**, 235701 (2011).
[42] S. C. Kapfer and W. Krauth, Phys. Rev. Lett. **114**, 035702 (2015).
[43] D. R. Nelson, Phys. Rev. B **27**, 2902 (1983).
[44] R. A. Serota, Phys. Rev. B **33**, 3403 (1986).
[45] S. Deutschländer, T. Horn, H. Löwen, G. Maret, and P. Keim, Phys. Rev. Lett. **111**, 098301 (2013).
[46] T. Nattermann, I. Lyuksyutov, and M. Schwartz, Europhys. Lett. **16**, 295 (1991).
[47] M. Mazars, Europhys. Lett. **110**, 26003 (2015).
[48] K. Zahn and G. Maret, Phys. Rev. Lett. **85**, 3656 (2000).
[49] M. D. Ediger, Annu. Rev. Phys. Chem. **51**, 99 (2000).
[50] R. Zangi and S. A. Rice, Phys. Rev. Lett. **92**, 035502 (2004).
[51] O. Dauchot, G. Marty, and G. Biroli, Phys. Rev. Lett. **95**, 265701 (2005).
[52] P. M. Reis, R. A. Ingale, and M. D. Shattuck, Phys. Rev. Lett. **98**, 188301 (2007).
[53] E. R. Weeks, J. C. Crocker, A. C. Levitt, A. Schofield, and D. A. Weitz, Science **287**, 627 (2000).
[54] W. Kob and H. C. Andersen, Phys. Rev. E **51**, 4626 (1995).
[55] W. Kob and H. C. Andersen, Phys. Rev. E **52**, 4134 (1995).
[56] C. Donati, J. F. Douglas, W. Kob, S. J. Plimpton, P. H. Poole, and S. C. Glotzer, Phys. Rev. Lett. **80**, 2338 (1998).
[57] P. Chaudhuri, L. Berthier, and W. Kob, Phys. Rev. Lett. **99**, 060604 (2007).
[58] O. Bohigas, S. Tomsovic, and D. Ullmo, Phys. Rep. **223**, 43 (1993).
[59] M. A. Reed and W. P. Kirk, *Nanostructure Physics and Fabrication* (Academic Press, Boston, 1989).
[60] R. C. Gann, S. Chakravarty, and G. V. Chester, Phys. Rev. B **20**, 326 (1979).
[61] H. Jiang, H. U. Baranger, and W. Yang, Phys. Rev. Lett. **90**, 026806 (2003).
[62] D. Ullmo, T. Nagano, and S. Tomsovic, Phys. Rev. Lett. **90**, 176801 (2003).
[63] D. Frenkel and B. Smit, *Understanding Molecular Simulation: From Algorithms to Applications*, 2nd ed. (Academic Press, San Diego, 2001).
[64] S. Kirkpatrick, C. D. Gelatt, and M. P. Vecchi, Science **220**, 671 (1983).
[65] To obtain the ground state ($T = 0$) configuration for Coulomb clusters, we have carried out Monte Carlo simulation following the procedure outlined in Ref. [19].
[66] D. R. Nelson, *Defects and Geometry in Condensed Matter Physics* (Cambridge University Press, Cambridge, UK, 2002).
[67] J. C. Tipper, Comput. Geosci. **17**, 597 (1991).
[68] M. Cerkaski, R. G. Nazmitdinov, and A. Puente, Phys. Rev. E **91**, 032312 (2015).
[69] M. Kong, B. Partoens, and F. M. Peeters, Phys. Rev. E **67**, 021608 (2003).
[70] A. E. Larsen and D. G. Grier, Phys. Rev. Lett. **76**, 3862 (1996).
[71] P. Dillmann, G. Maret, and P. Keim, J. Phys.: Condens. Matter **24**, 464118 (2012).
[72] K. H. Nagamanasa, S. Gokhale, R. Ganapathy, and A. K. Sood, Proc. Natl. Acad. Sci. U.S.A. **108**, 11323 (2011).
[73] C.-L. Chan, C.-W. Io, and L. I, Contrib. Plasma Phys. **49**, 215 (2009).
[74] J. P. Hansen and I. R. McDonald, *Theory of Simple Liquids*, 3rd ed. (Academic Press, San Diego, 2006).
[75] K. He, S. T. Retterer, B. R. Srijanto, J. C. Conrad, and R. Krishnamoorti, ACS Nano **8**, 4221 (2014).
[76] J. D. C. Jacob, K. He, S. T. Retterer, R. Krishnamoorti, and J. C. Conrad, Soft Matter **11**, 7515 (2015).
[77] S. Karmakar, C. Dasgupta, and S. Sastry, Annu. Rev. Condens. Matter Phys. **5**, 255 (2014).
[78] S. Karmakar, C. Dasgupta, and S. Sastry, Proc. Natl. Acad. Sci. U.S.A. **106**, 3675 (2009).
[79] C. Donati, S. Franz, S. C. Glotzer, and G. Parisi, J. Non-Cryst. Solids **307**, 215 (2002).
[80] The general functional dependencies are estimated by considering different realistic possibilities and choosing the one that minimizes χ^2 [89] of the best fit.
[81] L. Berthier and G. Biroli, Rev. Mod. Phys. **83**, 587 (2011).
[82] M. Khademi, R. K. Kalia, and M. Sahimi, Phys. Rev. E **92**, 030301 (2015).
[83] E. Rabani, J. D. Gezelter, and B. J. Berne, Phys. Rev. Lett. **82**, 3649 (1999).
[84] A. Shekhar, R. K. Kalia, A. Nakano, P. Vashishta, C. K. Alm, and A. Malthe-Srenssen, Appl. Phys. Lett. **105**, 161907 (2014).

[85] J. C. Phillips, Rep. Prog. Phys. **59**, 1133 (1996).
[86] P. Grassberger and I. Procaccia, J. Chem. Phys. **77**, 6281 (1982).
[87] L. O. Hedges, L. Maibaum, D. Chandler, and J. P. Garrahan, J. Chem. Phys. **127**, 211101 (2007).
[88] L. Berthier, D. Chandler, and J. P. Garrahan, Europhys. Lett. **69**, 320 (2005).
[89] W. H. Press, S. A. Teukolsky, W. T. Vetterling, and B. P. Flannery, *Numerical Recipes: The Art of Scientific Computing*, 3rd ed. (Cambridge University Press, New York, 2007).
[90] C. E. Lunneborg, *Ansari Bradley Test* (John Wiley & Sons, New York, 2005).
[91] Y. Ueno and S. Okamoto, Phys. Lett. A **85**, 103 (1981).